Encoding of task regularities links grid-like signals to human timing behavior

Ignacio Polti[1,2*], **Matthias Nau**[1,2*], **Raphael Kaplan**[1,3], **Virginie van Wassenhove**[4], **and Christian F. Doeller**[1,2,5,6]

[1]Kavli Institute for Systems Neuroscience, Centre for Neural Computation, The Egil and Pauline Braathen and Fred Kavli Centre for Cortical Microcircuits, Jebsen Centre for Alzheimer's Disease, Norwegian University of Science and Technology, Trondheim, Norway

[2]Max-Planck-Institute for Human Cognitive and Brain Sciences, Leipzig, Germany

[3]Department of Basic Psychology, Clinical Psychology, and Psychobiology, Universitat Jaume I, Castellón de la Plana, Spain

[4]CEA DRF/Joliot, NeuroSpin; INSERM, Cognitive Neuroimaging Unit; Université Paris-Saclay, Gif-Sur-Yvette, France

[5]Wilhelm Wundt Institute of Psychology, Leipzig University, Leipzig, Germany

[6]Department of Psychology, Technische Universität Dresden, Dresden, Germany

Shared-first authors

Abstract

Grid cells have been proposed to encode task regularities that allow predicting future states. Entorhinal grid-like signals might therefore mirror behavioral biases associated with relying on task regularities, like regression-to-the-mean biases in time estimation. Here, we tested this proposal using functional magnetic resonance imaging and a rapid timing task in humans. Indeed, trial-wise entorhinal activity reflected task accuracy and the degree to which interval estimates regressed towards the mean of all tested intervals. Grid-like signals were observed exclusively for the interval closest to the mean, which was explained by differences in temporal stability across intervals. Finally, both behavioral and entorhinal results were explained by a Bayesian observer model that assumes the integration of current-trial sensory evidence with prior expectations. Together, we find that entorhinal activity and grid-like signals reflect behavioral performance in a timing task, supporting the proposed role of grid cells in encoding task structure for predictive coordination of behavior.

ignacio.polti@ntnu.no, m.nau@vu.nl, doeller@cbs.mpg.de

1 Introduction

The ability to recognize and utilize statistical regularities governed by the co-occurrence of stimuli, actions, and events is crucial for any successful interaction with the environment (Vetter, Wolpert, 2000; Clark, 2013; Friston, Buzsáki, 2016). Learning about such regularities allows us to predict future states of the world, for instance to track moving objects during occlusion, which is an essential ability underlying flexible and robust behavior broadly (Fiser et al., 2010; Heald et al., 2023; Schapiro, Turk-Browne, 2015; Schapiro et al., 2016). When catching an approaching ball, for example, we anticipate the moment it will reach us not solely based on our estimates of its current speed and distance, but also based on our knowledge of how previous balls have behaved in similar situations. Through experience, we have learned about the probability associated with certain speeds and arrival times, which now guides when and how we act. How does the brain encode such statistical regularities and how do they afford predictive inference in the service of behavior?

A prominent metaphor of how the brain encodes statistical regularities can be found in the concept of cognitive maps, referring to relational map-like representations of places and events that support mnemonic and predictive processes (O'Keefe, Nadel, 1978; Moser et al., 2014; Stachenfeld et al., 2017; Whittington et al., 2020; Eichenbaum et al., 1999). A large body of neuroscientific literature on cognitive maps and predictions pointed to the hippocampal formation as a key neural component involved in both, fueling efforts to unify theories of its contribution to a range of tasks (Whittington et al., 2020; Stachenfeld et al., 2017; Ambrogioni, Ólafsdóttir, 2023; Behrens et al., 2018; Bellmund et al., 2018). An emerging view is that the hippocampal formation plays an important role in encoding regularities that afford generalization across tasks or contexts (e.g., different environments; Whittington et al. (2020); Bousquet et al. (1998); Fuhs, Touretzky (2007); Penny et al. (2013); Friston, Buzsáki (2016); Pezzulo et al. (2017)), thus greatly accelerating learning and reducing behavioral errors in novel or noisy situations (Lisman, Redish, 2009; Stachenfeld et al., 2017). In particular, the hippocampus has been suggested to support the encoding of task regularities in real time as a task is performed, as its activity reflects feedback and behavioral improvements even in fast-paced timing tasks (Polti et al., 2022).

Like the hippocampus, the entorhinal cortex is widely considered critical for cognitive mapping; not only is it a major anatomical gateway for hippocampal-cortical interactions (Witter, Amaral, 2004), but it also harbors grid cells (Hafting et al., 2005; Moser et al., 2014) proposed to provide a map-like coordinate system useful for representing relationships between places and events in the world (e.g., different spatial positions during navigation, but also non-spatial features (Constantinescu et al., 2016; Aronov et al., 2017; Behrens et al., 2018; Bellmund et al., 2018; Bao et al., 2019; Theves et al., 2019, 2020; Viganò, Piazza, 2020; Park et al., 2021). This grid-like coordinate system may be predictive in nature, meaning that it likely anticipates future states of the agent (e.g., future positions during navigation, Stachenfeld et al. (2017)) and affords efficient vector computations for spatial planning (Banino et al., 2018; Bush et al., 2015; Bicanski, Burgess, 2020). At the population level, grid cell activity is believed to exhibit a hexadirectional (i.e., six-fold rotationally symmetric) modulation as a function of virtual running or gaze direction (Killian et al., 2012), which can be observed in the human entorhinal cortex using functional magnetic resonance imaging (fMRI) (Doeller et al., 2010; Julian et al., 2018; Nau et al., 2018b). Importantly, while grid-like signals have been observed in a range of tasks and species (Kunz et al., 2019), most studies left open whether or not grid-like signals were indeed relevant for task performance.

Here, we set out to understand the contributions of the entorhinal cortex and grid-like signals in particular to the encoding of task regularities that afford predictive coordination of actions relative

to sensory events. In addition, we investigated the relationship between grid-like signals and task performance - a relationship that is often assumed but remains to be demonstrated empirically. For this purpose, we monitored human brain activity using fMRI while participants engaged in a visual tracking task previously shown to engage grid-like signals in the human entorhinal cortex (Nau et al., 2018b) as well as a time-to-contact (TTC) estimation task shown to engage the adjacent hippocampus in a rapid and behavior-dependent manner (Polti et al., 2022). We specifically tested whether and how entorhinal activity reflects behavioral biases previously linked to the encoding of timing-task regularities (Jazayeri, Shadlen, 2010), focusing on the posteromedial portion of the entorhinal cortex (pmEC); the presumed human homologue of the rodent medial entorhinal cortex that harbours grid cells (Navarro Schröder et al., 2015; Maass et al., 2015; Syversen et al., 2021).

Results

In the following, we will present our experiment and results in 5 steps. First, we introduce our task design and empirical measures in detail. Second, we show that task performance depended not only on the interval that was tested in each trial, but also on the intervals tested in previous trials, with behavioral responses showing a systematic bias towards the average interval. This regression-to-the-mean bias suggests that participants relied on prior knowledge that accumulated across trials. Third, we report that trial-wise pmEC activity mirrored this behavioral bias in real time, similar to previous reports for the hippocampus (Polti et al., 2022). Fourth, we show that human pmEC grid-like signals co-varied with the tested intervals across trials. This effect was explained by the temporal stability of the grid-like signal (i.e. replicability across data partitions), and its amplitude was correlated with behavioral performance in all participants. Finally, by showing that a Bayesian observer model provides a parsimonious account of the data, we illustrate a potential computational explanation of our results, namely that entorhinal grid-like signals may reflect the mismatch between prior knowledge and sensory evidence obtained in each trial. Collectively, these results suggest that non-spatial task factors (such as tested intervals) shape spatial representations in the entorhinal cortex in service of timing behavior, and that entorhinal activity, and grid-like signals in particular, reflect the rapid encoding of task regularities in service of predictive inference. Moreover, our results also provide evidence for a link between grid-like signals and task performance.

Time-to-contact (TTC) estimation task

Our task consisted of two components; a visual tracking task that engages grid-like signals in the human EC (Nau et al., 2018b), as well as a predictive timing task that engages other regions including the adjacent hippocampus (Polti et al., 2022). Over the course of 768 trials, participants tracked a moving fixation target with their eyes until it was occluded, which then prompted them to predict when the target would hit a visual boundary. In each trial, the fixation target moved 10 degrees of visual angle (dva) into one of 24 directions (Fig. 1A, "Gaze trajectory") at one of 4 possible speeds, yielding 4 different intervals to be estimated (t_{TTC}): 0.55, 0.65, 0.86, and 1.2 s (See *Methods*). Speed and direction were held constant within each trial. After the target stopped moving, participants estimated the time when it would have hit the visual boundary 5 dva apart, which they indicated via button click (Fig. 1A, "TTC estimation"). Participants then received feedback reflecting the accuracy of their estimated TTC relative to the ground-truth TTC. The next trial then started after a jittered inter-trial interval (ITI). See the methods section for details.
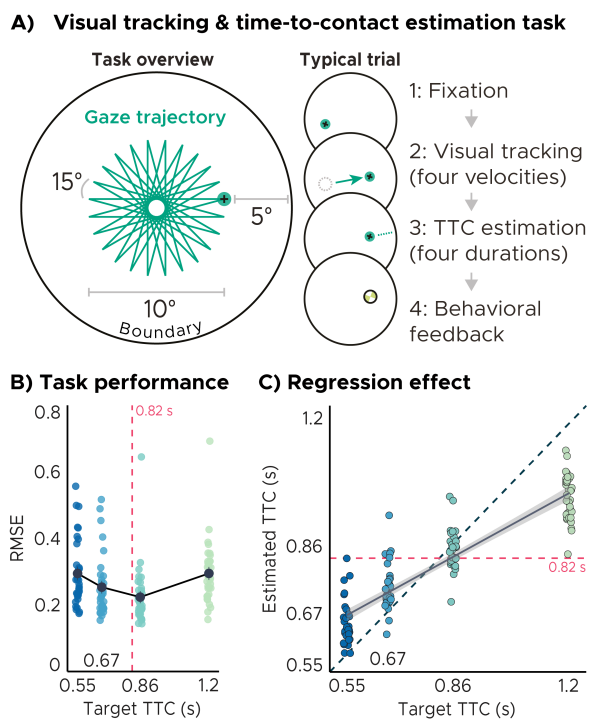
Figure 1: A) Visual tracking and Time-To-Contact (TTC) estimation task. In each trial during fMRI scanning, participants fixated on a target (1), which started moving at one of 4 possible speeds and in one of 24 possible directions for 10 dva (2). After the target stopped moving, participants kept fixating and estimated when the fixation target would have hit a boundary 5 dva apart (3). After pressing a button at the estimated TTC, participants received feedback (4) based on their performance. **B)** Task performance. Root-mean-square error (RMSE) differences across TTCs show a quadratic pattern, i.e. target TTCs closer to the mean of the sampled TTCs (vertical dashed line) have a lower RMSE. We plot the mean and SEM (black dot and line). **C)** Regression effect. Participants responses regressed towards the mean of the sampled TTCs (0.82, horizontal dashed line), away from the identity line (diagonal dashed line). Regression line (black) and standard error (gray shade). **BC)** Single-participant data plotted as dots. Target TTCs are color coded.

Behavioral results

To examine whether participants performed the task well, we first compared their estimated TTC to the target TTC (ground truth) using a mixed-effects model (MEM). Indeed, we found that the estimated and target TTCs were tightly correlated (Fig. 1C; $F(1) = 976.44, p = 2.2x10^{-16}, \epsilon^2 = 0.91, CI : [0.88, 1]$). However, TTC estimates were further systematically biased towards the mean of the tested intervals (0.82 s, Fig. 1C, horizontal dashed line) in line with previous reports using interval timing tasks (Miyazaki et al., 2005; Jazayeri, Shadlen, 2010; Acerbi et al., 2012; Cicchini et al., 2012; Chang, Jazayeri, 2018). We quantified this regression-to-the-mean bias by fitting a line to the TTC estimates on group-level, which resulted in a slope value of 0.53 (Fig. 1C, MEM fit, diagonal solid line). For comparison, perfect task performance would lead to a slope of 1, whereas total regression to the mean would result in a slope of 0.

To quantify task performance in more detail, we then calculated the precision and accuracy in TTC estimation for each participant and time interval. Precision describes how similar the estimates were across trials, whereas accuracy describes how similar they were to the ground-truth target TTC (see methods for details). Together, these two measures combine into the root-mean-square error (RMSE), which we computed as our final performance measure. Note that a given RMSE can be the result of different precision-accuracy trade-offs (Fig. S1A). We found that the RMSE showed a quadratic relationship to the t_{TTC}, meaning that lower RMSE's were observed for t_{TTC} closer to the mean of the tested intervals (Fig. 1B; MEM, $F(2) = 39.18, p = 1.5x10^{-9}, \epsilon^2 = 0.68, CI : [0.52, 1]$). This quadratic trend explained the data better than assuming a linear trend (Chi-square test, $\chi^2(3) = 66.15, p = 2.85x10^{-14}$).

Taken together, our behavioral results showed that participants performed the task well (Fig. 1B, C), and that their TTC estimates exhibited systematic regression-to-the-mean biases (Fig. 1C). These biases are well documented in the literature and suggest that participants relied on prior knowl-

111 edge beyond the current trial to estimate time (Miyazaki et al., 2005; Jazayeri, Shadlen, 2010; Acerbi
112 et al., 2012; Cicchini et al., 2012; Chang, Jazayeri, 2018; Meirhaeghe et al., 2021; Polti et al., 2022).

Entorhinal cortex activity reflects trial-wise accuracy and biases in TTC estimation

114 Previous work on the present data showed that activity in the hippocampus reflected the mag-
115 nitude of the behavioral regression-to-the-mean effect across trials (Polti et al., 2022). Here, we
116 therefore first tested whether a similar effect can be observed for the pmEC. Using mass-univariate
117 general linear models (GLM), we modeled the activity in each trial parametrically either as a func-
118 tion of accuracy (i.e., the absolute difference between estimated and target TTC; Fig. 2A, top) or as a
119 function of the magnitude of the regression effect (i.e., the absolute difference between estimated
120 TTC and the mean of the tested intervals; Fig. 2A, bottom). To avoid effects of potential colinearity
121 on the final parameter estimates, these two predictors were fit in two independent GLMs, which in-
122 cluded additional nuisance predictors (e.g., for head-motion, see methods). We found that pmEC
123 activity was higher in trials in which TTC estimates were more accurate (Fig. 2B, left; two-tailed
124 one-sample Wilcoxon signed-rank test; $V = 89, p = 1.8x10^{-4}, r = -0.70, CI : [-0.85, -0.45]$), but also
125 that it linearly increased with stronger regression-to-the-mean biases (Fig. 2B, right; two-tailed one-
126 sample Wilcoxon signed-rank test; $V = 157, p = 0.015, r = -0.47, CI : [-0.72, -0.13]$), resembling the
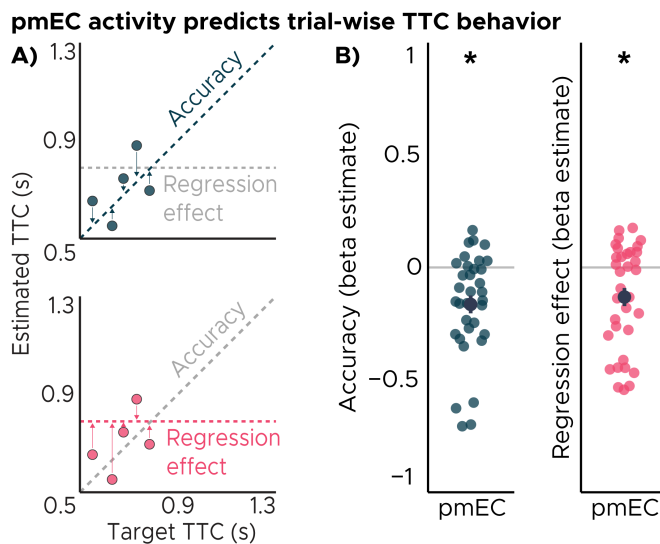127 effects previously reported for the hippocampus (Polti et al., 2022).

pmEC activity predicts trial-wise TTC behavior

Figure 2: **Posteromedial entorhinal cortex (pmEC) activity predicts trial-wise TTC behavior.** A) Schematic description of the parametric regressor (PR) used in each separate GLM. The Accuracy PR (Top) contained the absolute difference between estimated TTC and the identity line for each trial (petrol diagonal dashed line), whereas the Regression effect PR (Bottom) contained the absolute difference between estimated TTC and mean of the tested TTCs (0.82, magenta horizontal dashed line). B) Independent regions-of-interest analysis for pmEC. We plot the beta estimates obtained for each participant for each of the two regressors. Negative values indicate higher pmEC activity with either higher accuracy (left) or higher magnitude of the regression effect (right). Depicted are the mean and SEM across participants (black dot and line) overlaid on single participant data (colored dots). Statistics reflect p<0.05 (*) obtained using a group-level two-tailed one-sample Wilcoxon signed-rank test against zero.

Entorhinal grid-like signals predict behavioral performance in time estimation

129 The results reported above indicate that trial-wise pmEC activity was associated with the accuracy
130 and the bias in TTC estimation. However, these analyses do not address whether or not grid-like
131 signals show an association to our behavioral measures as well. Therefore, we next examined grid-
132 like signals in our data separately for each t_{TTC} using an established quadrature filter approach
133 (Doeller et al., 2010). The aim of this analysis was to examine whether pmEC voxels exhibited
134 visual grid-like signals in our task (i.e., six-fold rotationally symmetric modulations as a function of
135 gaze direction (Nau et al., 2018b; Julian et al., 2018; Staudigl et al., 2018)), and if so, whether these
136 signals show a relationship to the regression-to-the-mean bias as well.

137 We split the time series of each pmEC voxel into two halves for later cross-validation, and then
138 modeled each of the halves separately using a voxel-wise GLM. The GLM included two parametric
139 main predictors modeling the sine and cosine of gaze direction modulo 60° (Fig. 3A) in addition to
140 nuisance regressors (see methods). The ratio between the beta estimates obtained for these two
141 predictors then allowed us to infer the putative grid orientation (i.e., the phase of the hexadirec-
142 tional modulation) for each voxel, which were then averaged across voxels and across scanning
143 runs within each data partition. This procedure resulted in one putative grid-orientation for each
144 t_{TTC} and each data partition. Using a second GLM, we then tested the reliability of these grid-like
145 signals in the respective held-out data by modeling the activity of each voxel as a function of gaze di-
146 rection aligned with the putative grid orientation modulo 60°. In other words, the predictor tested
147 whether MRI signals observed for gaze directions aligned with the putative grid orientation were
148 stronger than those observed for directions misaligned to it.

149 We found that pmEC indeed exhibited a reliable grid-like modulation in our task as indicated by
150 a regions-of-interest (ROI) analysis. Critically, however, we observed a main effect of t_{TTC} on the
151 amplitude of this grid-like modulation (Fig. 3B; MEM, $F(3) = 3.08, p = 0.029, \epsilon^2 = 0.04, CI : [0, 1]$),
152 with only one of the four tested intervals showing the effect ($TTC_{0.86}$, Fig. 3B; Table S1). Trials in
153 which $TTC_{0.86}$ was tested yielded a stronger grid-like signal than all other TTCs (Table S1). Note
154 that $TTC_{0.86}$ was the interval that was closest to the mean of all intervals. A whole-brain voxel-wise
155 analysis later confirmed that this grid-like modulation for $TTC_{0.86}$ occurred in both hemispheres in
156 the entorhinal cortex (Fig. 3C, left and middle panels) as well as in a few other regions that shared
157 the putative grid orientation with the pmEC (e.g., the pre-supplementary motor area (preSMA), Fig.
158 3C, right panel; see Table S2 for post-hoc ROI-analysis). No effect was observed in pmEC when the
159 same cross-validation analysis was repeated for other directional periodicities such as 90° (Fig. 3D,
160 Left; Table S3A) and 45° (Fig. 3D, Center; Table S3B). Furthermore, as expected based on previous
161 work Nau et al. (2018b), the early visual cortex did not exhibit a grid-like signal (Fig. 3D, Right; Table
162 S3C).

163 Having established that pmEC activity was modulated in a grid-like fashion for one of the TTCs, we
164 next sought to understand the underlying differences across TTCs in more detail. Previous studies
165 using navigation paradigms (Kunz et al., 2015; Stangl et al., 2018) suggested that these differences
166 in grid-like signals may be due to (i) differences in spatial stability (i.e., grid orientations may differ
167 across voxels and therefore average out), or (ii) differences in temporal stability (i.e., grid orienta-
168 tion may change over the course of the experiment). To test whether any one of these factors could
169 explain the pattern of results in our data, we estimated the spatial and temporal stability of the
170 pmEC grid-like signal for each of the 4 TTCs separately. We found that grid orientations clustered
171 across pmEC voxels for all t_{TTC} in a similar way (Fig. S3B; Table S4A), ruling out differences in spatial
172 stability between t_{TTC} (Fig. S3B; MEM, $F(3) = 0.36, p = 0.78, \epsilon^2 = -0.02, CI : [0, 1]$). However, tempo-
173 ral stability predicted the amplitude of grid-like signals, which means that the more pmEC voxels
174 showed a stable grid orientation over data partitions, the stronger the resulting cross-validated
175 signal amplitude turned out to be (Fig. 3E; Spearman's $rho = 0.57, p = 5x10^{-4}$). Furthermore, as ex-
176 pected based on the results for grid-like signal amplitude, $TTC_{0.86}$ trials showed the highest tempo-
177 ral stability among all tested t_{TTC} (Fig. S3A; Table S4B, MEM, $F(3) = 3.49, p = 0.018, \epsilon^2 = 0.05, CI : [0, 1]$).

178 These findings provide evidence that pmEC grid-like signal amplitude differed across tested inter-
179 vals, and that this difference was largely explained by how stable the putative grid orientation was
180 over time. Importantly, we observed the grid-like signal only for the interval closest to the mean
181 of all intervals. This result dovetails with our prior observation that trial-wise pmEC activity cor-
182 related with how strongly behavioral responses were biased towards the mean interval (Fig. 2),

183 and it suggests that grid-like signals may also show a relationship to behavioral performance in
184 our task, which was indeed the case. In all of our participants, the grid-like signal amplitude was
185 negatively and linearly related to timing performance, meaning that TTCs with lower RMSE showed
186 the strongest grid signals (Fig. 3F; MEM, $F(3) = 10.1, p = 0.004, \epsilon^2 = 0.28, CI : [0.07, 1]$). Again, this
187 result was not observed for early visual cortex (V1, Fig. S3D; MEM, $F(3) = 2.6, p = 0.125, \epsilon^2 = 0.13, CI :$
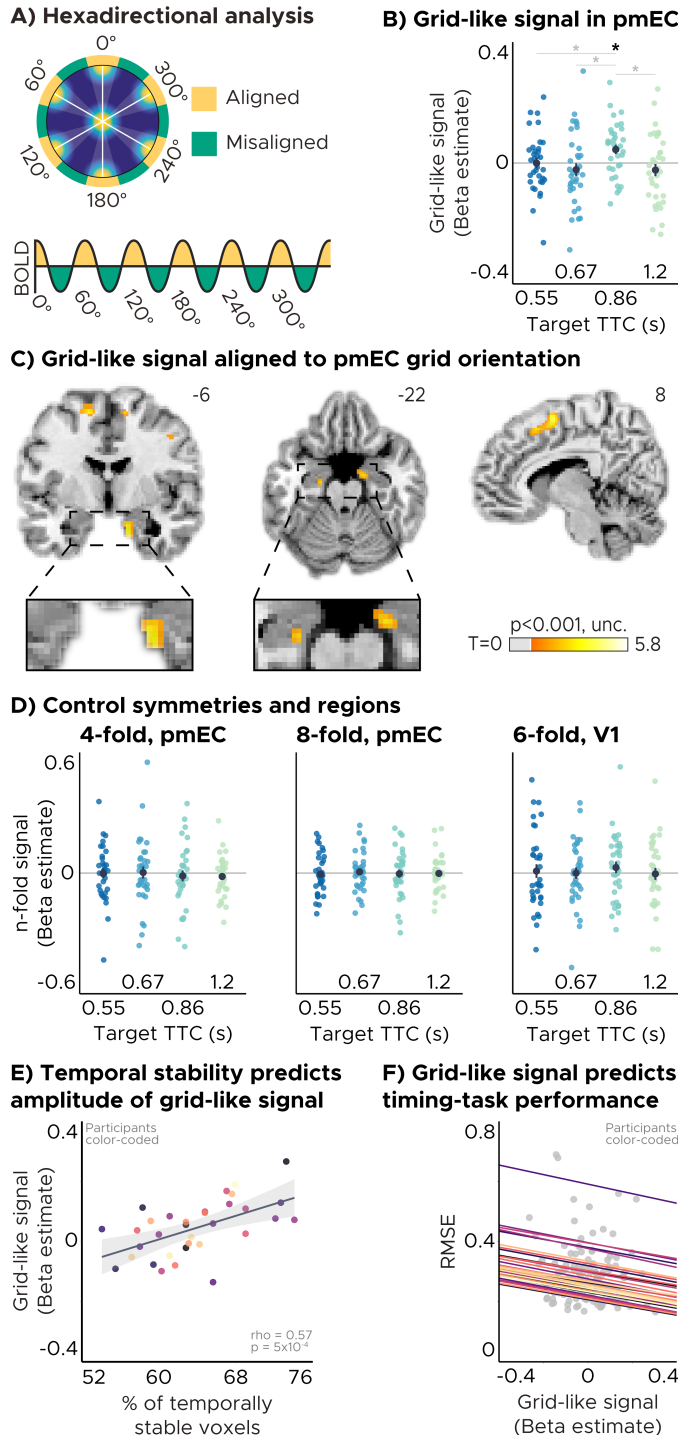188 $[0.0, 1]$).

Figure 3: A) Visual grid-like analysis method. The hexadirectional signal is cross-validated across data partitions. Putative grid-orientation was estimated using half of the data and then used to contrast orientation-aligned vs. orientation-misaligned gaze movements in the other half (odd vs. even runs). B) Independent regions-of-interest (ROI) analysis for 6-fold symmetry in pmEC. We plot the amplitude of the hexadirectional signal in held-out data expressed as beta estimate. We found reliable cross-validated hexadirectional modulation at the group level only for $TTC_{0.86}$ trials. There were consistent differences in pmEC fMRI activity for aligned vs. misaligned directions across target TTCs. Statistics reflect $p<0.05$ at FDR-corrected levels (*). C) Voxel-wise analysis results exhibiting activity modulation by gaze movement direction with 60° periodicity aligned to the pmEC grid orientation for $TTC_{0.86}$ trials. We plot thresholded t-test results at 2mm resolution at $p < 0.001$ uncorrected levels overlaid on a structural template brain. Insert zooming in on EC and MNI coordinates added. D) Control symmetries and regions. Left: 4-fold symmetry in pmEC. Center: 8-fold symmetry in pmEC. Right: 6-fold symmetry in V1. E) $TTC_{0.86}$ pmEC temporal stability predicts corresponding grid-like modulation across participants. Each dot represents a single participant. Regression line (black) and standard error (gray shade). F) Within-subject pmEC grid-like modulation predicts TTC estimation error (RMSE). Stronger pmEC grid-like modulation elicited lower RMSE. Separate regression lines are plotted for each participant. B,D) Depicted are the mean and SEM across participants (black dot and line) overlaid on single participant data (colored dots). Target TTCs are color coded. EF) Participants are color coded.

A Bayesian observer model explains performance differences across target TTCs

The behavioral and physiological results presented above suggest that participants' interval estimates depended on both the current trial and previous trials. This pattern of results is reminiscent of prior work on Bayesian integration (Körding, Wolpert, 2004; Petzschner et al., 2015), which has indeed been argued to underlie contextual effects in interval timing (Jazayeri, Shadlen, 2010; Acerbi et al., 2012; Cicchini et al., 2012). According to the Bayesian framework, the regression-to-the-mean effects we observed at the behavioral level (Fig. 1C) may be a natural consequence of integrating the sensory evidence in each trial (i.e., the inferred probability of a certain TTC being tested) with an expectation informed by the statistical regularities governing prior trials (i.e., the inferred prior distribution of all tested intervals), leading to the characteristic behavioral biases towards the mean of the encoded interval distribution. A Bayesian observer model may therefore provide a parsimonious computational explanation of both the behavioral regression-to-the-mean effect (Fig 1C) and the observed difference in grid-like activity across TTCs (Fig. 3B).

We tested this possibility post-hoc using a Bayesian observer model that was successfully used to model timing behavior in previous work (Jazayeri, Shadlen, 2010, 2015; Remington et al., 2018; Chang, Jazayeri, 2018). Briefly, the model predicts the optimal TTC estimate for each trial by combining two sources of information: (i) the probability that a specific TTC was tested in a trial given the sensory evidence obtained during the visual tracking phase (Likelihood, Fig. 4A Left), and (ii) a Gaussian prior centered on the mean of the sampled intervals (Prior; Fig. 4A Left). For each participant, a separate model was trained and tested using cross-validation, which built on fitting the model on one half of the data and predicting TTC estimates in the remaining half (see Methods for details).

In line with previous work (Jazayeri, Shadlen, 2010, 2015; Remington et al., 2018; Chang, Jazayeri, 2018), we found that the model accurately predicted participants' interval estimates across trials (Fig. 4B), with a group average Mean Absolute Error (MAE) of 0.02. The model further recapitulated each participant's task-performance measures (Fig. 1B), with model-derived RMSE values following a quadratic pattern across t_{TTC} similar to the data (Fig. 4C; MEM, $F(2) = 74.95, p = 3.4x10^{-13}, \epsilon^2 = 0.8, CI : [0.7, 1]$). Moreover, by relating the model estimates to the neuroimaging results obtained for pmEC, we found that model-derived RMSE values were indeed correlated with the amplitude of grid-like signals observed in all participants (Fig. 4D; MEM, $F(1) = 8.15, p = 0.008, \epsilon^2 = 0.22, CI : [0.03, 1]$). Together, these modeling results suggest that the differences in participants' TTC estimates and in grid-like signals across TTCs can indeed be well explained using a Bayesian observer model that assumes that predictions informed by temporal regularities in previous trials bias timing behavior in the current trial.

One notable assumption of the model was that the prior distribution of intervals was centered on the mean of the sampled intervals. To test whether this assumption was valid, we ran the model four times, each time centering the prior close to one of the four tested intervals (Fig. S4). Centering the prior on a value far from the mean interval could in theory result in an even better fitting model and a closer match to our behavioral data. However, we found both the model fit (Fig. S4C, Table S5) and the match between model-derived and real task performance (Fig. S4D) to be optimal when the prior was assumed to be centered on the mean interval. Consequently, only the model with a prior centered on the mean interval recapitulated the quadratic RMSE pattern across t_{TTC} we observed in the data (Fig. S4D).
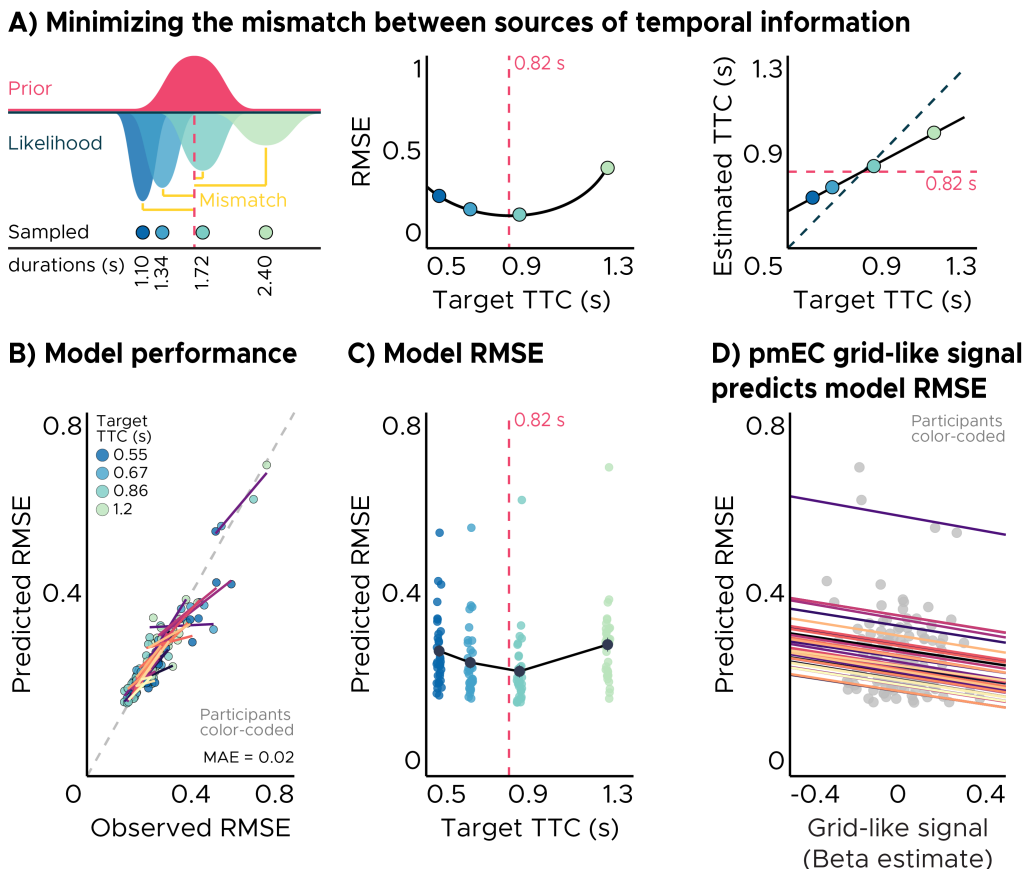
Figure 4: A) Schematic illustration of Bayesian TTC estimation. Left: A Bayesian observer integrates sensory Likelihood and Prior information sources to minimize their mismatch (yellow lines). One source of information comes from a prior expectation (Prior, magenta Gaussian distribution), centered at the mean of the sampled durations (magenta horizontal dashed line). Another source of information comes from noisy sensory inputs (Likelihood, Gaussian distributions of different widths and turquoise tones). On each trial, by combining these two information sources participants can produce a statistically optimal *Estimated TTC*. Center: An optimal Bayesian estimator that minimizes the mismatch between Prior and Likelihood would be expected to show a Root-Mean-Square-Error (RMSE) pattern across target TTCs best explained by a quadratic function (solid green line). The RMSE increases quadratically as a function of the Target TTC's distance to the mean of the prior (magenta vertical dashed line, 0.82 s). Right: As a result of the integration of these two sources of information, TTC estimates are biased 'away' from the identity line (petrol blue diagonal dashed line) and 'towards' the mean of the sampled TTCs (magenta horizontal dashed line). B) Bayesian observer model performance. We plot the cross-validated model prediction vs. participants' data. The model successfully captures participants' behavior, with a Mean Absolute Error (MAE) of 0.02. Colored lines represent participants' linear model fits across Target TTCs. For most participants the linear model fits are well aligned with the identity line (diagonal grey dashed line). C) Model RMSE per target TTC. Predicted participants' behavior using the cross-validated Bayesian observer model. RMSE differences across TTCs show a quadratic pattern, replicating real participants' behavior (Fig. 1B). D) As expected, participants' pmEC grid-like signals predict model's RMSE, replicating our experimental observations (Fig. 3F). BC) Target TTCs are color coded. Single-participant data plotted as dots. BD) Separate regression lines are plotted for each participant.

Discussion

The present study examined whether and how the human pmEC contributes to the encoding of task regularities that guide timing behavior. We used fMRI to record human brain activity while participants performed a rapid time-to-contact estimation task, which allowed us to analyze trial-wise pmEC activity as a function of time-estimation performance across a range of sampled intervals. Moreover, the task included periods in which participants followed a moving fixation target with their eyes, allowing us to estimate visual grid-like signals in the pmEC: the amplitude and stabil-

239 ity of a six-fold rotationally symmetric MRI-signal modulation as a function of gaze direction. We
240 found that pmEC activity closely tracked task performance across trials as well as behavioral re-
241 sponse biases towards the mean interval, and we observed a bias towards that mean interval on
242 the level of grid-like signals. Traditionally, such regression-to-the-mean biases have been taken as
243 evidence for Bayesian integration in the brain (Petzschner et al., 2015), since they are well explained
244 by models that assume the integration between sensory evidence obtained in a trial with a prior
245 expectation derived from previous trials. Indeed, a Bayesian observer model previously used to
246 model timing behavior in humans and macaques (Jazayeri, Shadlen, 2010, 2015; Remington et al.,
247 2018; Chang, Jazayeri, 2018; De Kock et al., 2021) provided a parsimonious account for both our
248 behavioral and pmEC results. In the following, we will discuss these results in light of previous liter-
249 ature on timing behavior and relate them to prior work on spatial and non-spatial coding principles
250 in the hippocampal formation.

Task regularities bias TTC estimation in future trials

252 While participants were not explicitly told about the true range of intervals that were tested, their
253 estimates were nevertheless biased towards the mean interval (Fig. 1B, C). This regression-to-the-
254 mean effect in time estimation is well documented and has been proposed to reflect participants'
255 reliance on the temporal regularities learned from previous trials (Miyazaki et al., 2005; Jazayeri,
256 Shadlen, 2010; Acerbi et al., 2012; Cicchini et al., 2012; Petzschner et al., 2015; Chang, Jazayeri,
257 2018; Polti et al., 2022). Specifically, integrating a prior expectation with the sensory evidence ob-
258 tained in the current trial may help participants to anticipate the trajectory of moving objects during
259 occlusion (Fig. 4A). This prior expectation likely takes the form of a Gaussian distribution of time
260 intervals centered on the mean (Fig. S4D). Relying on this prior to make an interval judgement
261 will therefore most often be biased towards that mean, depending on how strong the sensory evi-
262 dence is in a given trial about the true TTC that was tested. With increased mismatch between prior
263 expectation and sensory evidence, participants' estimates may be biased more towards the mean
264 (Fig. 1B, C), potentially reflecting an increase in uncertainty about their estimate (Jazayeri, Shadlen,
265 2010; Petzschner et al., 2015). Overall, this strategy may lead to large errors in some trials, but it
266 may nevertheless be adaptive, since the mean is still a "good guess" for the large majority of trials.
267 This is especially true for those trials in which the evidence derived from the senses is sparse or
268 noisy. Interestingly, we tested only four intervals drawn from a uniform distribution, meaning that
269 the mean interval does not actually account for a large proportion of the trials. However, previous
270 work has shown that interval estimates tend to be encoded using a Gaussian distribution even
271 when the intervals were sampled uniformly (Acerbi et al., 2012), in line with our observation that
272 our data was well described using a Bayesian model that assumed a Gaussian distribution centered
273 on the mean interval (Fig. 4).

Entorhinal cortex encodes task regularities that afford time estimation

275 Entorhinal activity reflected the behavioral response biases towards the mean across trials, as well
276 as overall task performance. In our view, this result is striking in our view as the functions of the
277 entorhinal cortex are mostly studied in the context of spatial navigation (Epstein et al., 2017; Kunz
278 et al., 2019) and long-term memory formation (Fernández et al., 1999; Hargreaves et al., 2012;
279 Staresina et al., 2013; Schiller et al., 2015), not in the context of rapid timing tasks. Notably, similar
280 tasks have been used successfully for studying predictive processes in rodents (Henke et al., 2021),
281 humans (Jazayeri, Shadlen, 2010; Acerbi et al., 2012; Cicchini et al., 2012; Chang, Jazayeri, 2018;
282 Polti et al., 2022), and non-human primates (Jazayeri, Shadlen, 2015; Wang et al., 2018; Sohn et al.,

283 2019), but not in the context of entorhinal functions. Our results suggest that computations in the
284 human entorhinal cortex contribute to timing task performance in real time as the task is being
285 performed. In fact, we found trial-wise pmEC activity to follow a pattern that closely resembled the
286 one previously reported for the adjacent hippocampus, as well as for other regions prominently
287 including the striatum (Polti et al., 2022; Rolando et al., 2024). The contributions of the entorhinal
288 cortex to task performance may therefore closely depend on other regions shown to preferentially
289 encode distinct behaviorally relevant factors, such as task details versus task structure (Doeller
290 et al., 2008; Geerts et al., 2020). Specifically, the hippocampal-entorhinal region has been shown
291 to signal the encoding of task structure (e.g., graphs reflecting transition probabilities between se-
292 quentially presented stimuli (Garvert et al., 2017)) and abstract task spaces (Constantinescu et al.,
293 2016; Theves et al., 2019, 2020; Viganò, Piazza, 2020; Park et al., 2021), which may reflect the learn-
294 ing of generalizable principles that guide behavior across tasks. Our results are in line with these
295 ideas and support recently proposed computational accounts of entorhinal function that center
296 on structured, factorized representations allowing inference and generalisation (Whittington et al.,
297 2020).

298 Our results further dovetail with work on temporal-context encoding (Schapiro et al., 2012; Hsieh
299 et al., 2014) and sequence memory (Fortin et al., 2002; Montchal et al., 2019; Bellmund et al., 2020a,
300 2022) in the hippocampal-entorhinal region. For example, animal studies have shown that damage
301 to the entorhinal cortex impairs memory for relations (Buckmaster et al., 2004), and inactivation
302 of the rodent MEC prevents context-dependent learning of intervals (Bigus et al., 2023). In general,
303 recent years have seen a growth in the literature on the links between MEC and timing behavior in
304 rodents (Heys, Dombeck, 2018; Heys et al., 2020; Vo et al., 2021; Dias et al., 2021; Bigus et al., 2023).
305 Our results extend these reports to the human pmEC, revealing a direct relationship between pmEC
306 activity and behavioral performance in a timing task. Specifically, its activity mirrored a behavioral
307 bias towards the mean of the tested intervals; a phenomenon that occurs for any type of magni-
308 tude estimation (Petzschner et al., 2015; Petzschner, Glasauer, 2011). Investigating the relationship
309 between these mean biases and neural activity across a range of tasks therefore provides fertile
310 ground for investigations of the domain-general functions of the hippocampal-entorhinal region
311 (Behrens et al., 2018; Bellmund et al., 2018; Stachenfeld et al., 2017). In line with this idea, hip-
312 pocampal activity has been linked to regression-to-the-mean biases during the estimation of spa-
313 tial distances (Wiener et al., 2016) and intervals (Polti et al., 2022), and entorhinal activity has been
314 shown to be modulated by spatial context during virtual navigation (Julian, Doeller, 2021).

Non-spatial task factors shape entorhinal grid-like signals

316 In addition to co-variations in pmEC activity and task-performance measures across trials, we found
317 that pmEC grid-like signals in particular reflected participants' performance across intervals (Fig. 3F).
318 Like behavioral performance, also the grid-like signal seemed to be biased towards the mean inter-
319 val, with cross-validation revealing a robust grid-like modulation exclusively for the interval closest
320 to the mean. This effect was driven by the temporal stability, not spatial stability, of the grid-like
321 signal (Figs. S3A, B), in line with previous reports (Kunz et al., 2015; Stangl et al., 2018). Furthermore,
322 our results also replicate previous work on visual grid-like signals in humans (Nau et al., 2018b; Ju-
323 lian et al., 2018; Staudigl et al., 2018), while going beyond these studies by reporting a relationship
324 between these signals and behavioral performance. Eye movements may engage similar processes
325 in the entorhinal cortex as navigation (Nau et al., 2018a), while offering higher experimental con-
326 trol and study-design efficiency. Since behavioral performance was well explained by a Bayesian
327 observer model, we tested whether this model also predicted the grid-like signal differences across

intervals, which was indeed the case (Fig. 4C). Cross-validated model predictions recapitulated the link between task performance and the grid-like signal differences across intervals, potentially offering a parsimonious and normative explanation of our findings. The entorhinal cortex, and grid cells in particular, may support the encoding of task regularities that ultimately manifest in both neural activity and behavior as regression-to-the-mean effects.

Why would a spatial grid-like signal be modulated by the range of intervals that was tested? Previous work has shown that task-dependent factors such as environmental features, goal locations, and rewards can distort the grid-cell pattern in rodents (Barry et al., 2007, 2012; Krupic et al., 2015; Hardcastle et al., 2015; Keinath et al., 2018; Boccara et al., 2019; Butler et al., 2019), as well as grid-like (Viganò et al., 2023) and behavioral (Bellmund et al., 2020b; Chen et al., 2015) response patterns in humans. It therefore seems plausible that also human grid-like signals can be modulated by behaviorally-relevant features of the task. In our task, the most relevant feature was the intervals that were tested, possibly explaining why the timing error was lowest (Fig. 1C) and the temporal stability of the grid-like signal was highest (Fig. S3A) for the interval closest to the mean. Previous work suggested that the distortions of the grid-cell patterns could be the consequence of conflicting sources of information (Barry et al., 2007; Hardcastle et al., 2015; Krupic et al., 2015), which would be broadly in line with our Bayesian modeling results (Fig. 4). In our case, the conflicting sources of information may be the prior expectation derived from previous trials, which is inherently biased towards the mean interval, and the current-trial evidence derived from the senses. Therefore, we speculate that the amplitude and orientation of grid-like signals depend on the agreement between these two sources of information. This alignment becomes higher the closer the tested interval is to the mean interval.

Predictive processing as a domain-general principle of entorhinal function?

While many of the above considerations remain to be tested, it has long been recognized that learning task regularities ultimately requires the encoding of relationships between stimuli, actions, and events (Körding, Wolpert, 2004; Petzschner, Glasauer, 2011; Petzschner et al., 2015), which has been proposed to build on a relational coding scheme that has often been discussed for the medial temporal lobe (Manns, Eichenbaum, 2006; Whittington et al., 2020) even for non-spatial feature spaces (e.g., Aronov et al. (2017); Bellmund et al. (2018); Behrens et al. (2018); Constantinescu et al. (2016); Bao et al. (2019); Theves et al. (2019, 2020); Viganò et al. (2021); Park et al. (2021); Wagner et al. (2023); Nitsch et al. (2023)). Our task explicitly required participants to make temporal predictions, but the central ideas and observations presented in this article may therefore very well translate also to other tasks and less explicit situations. Taking a predictive-processing perspective may more generally help to understand the functional contributions of the entorhinal cortex across behavioral domains and species (e.g., Cothi de et al. (2022)), which includes, but is not limited to, the Bayesian framework. In fact, a growing number of studies support the idea that Bayesian models can provide a normative explanation for a range of observations in the spatial navigation literature, including the integration of visual cues and landmarks during path integration (Cheng et al., 2007; Petzschner, Glasauer, 2011; Kessler et al., 2022). Intriguingly, the same Bayesian model (Kang et al., 2023) that explains distortions in spatial memory in humans (Hartley et al., 2004; Chen et al., 2015; Bellmund et al., 2020b; Keinath et al., 2021) can also explain distortions of the grid-cell pattern in rodents (e.g., Krupic et al. (2015)), pointing towards a unified computational account for behavior and entorhinal activity across species.

Predictions for future work

Our results suggest that non-spatial task factors shape human entorhinal activity in real time as the task is performed, a phenomenon that future studies should investigate across a range of tasks. It is important to note that we modeled our results using a Bayesian observer model due to its successful application to similar problems in the past (Jazayeri, Shadlen, 2010; Acerbi et al., 2012; Remington et al., 2018; Chang, Jazayeri, 2018), but other computational frameworks may be able to explain our data equally well. Approaches that model the mismatch between prior expectations and sensory evidence more explicitly seem especially promising in this context (e.g., prediction errors in reinforcement learning (Momennejad et al., 2017; Niv, 2009; Dayan, Daw, 2008; Stachenfeld et al., 2017)). Second, our results are in line with the idea that participants encoded the tested intervals using a Gaussian distribution centered on the mean intervals, but a more fine-grained sampling of intervals would be necessary to convincingly show that this was actually the case. The ideal scenario would be to sample many more time intervals, not from one but from multiple distributions, each centered on a different value. In this case, one would predict that the grid-like signal is stable at the center of each of these distributions. Finally, to investigate the range of non-spatial factors that affect grid-like signals, and therefore to understand potential domain-general contributions of the pmEC to human cognition, future work should test a range of tasks beyond time estimation and spatial navigation.

Conclusion

Taken together, using fMRI and a rapid time-to-contact estimation paradigm in humans, we showed that time estimates are biased towards the mean of the tested intervals, and that this mean bias is reflected in entorhinal activity across trials (similar to the hippocampus, Polti et al. (2022)). Moreover, we report a novel relationship between grid-like signals and behavioral performance, as the amplitude of the grid-like signal correlated with participants' time-estimation error, and the putative grid orientation was stable exclusively for the interval closest to the mean. Finally, both our behavioral and neuroimaging results were well explained (post hoc) by a Bayesian observer model that assumes the integration of prior expectations and sensory evidence in each trial. These results point to an involvement of the pmEC in interval timing, likely building on the encoding of task regularities that afford predictive inference in the service of goal-directed behavior.

Acknowledgements

Author Contributions

MN, IP and CFD conceived the study. IP and MN designed the experimental paradigm, visualized the results, and embedded them in the literature with help from RK, VW and CFD. IP implemented

413   the experimental code and acquired and analyzed the data with close supervision from MN. MN
414   and IP wrote the manuscript with critical feedback from RK, VW, and CFD. CFD provided general
415   supervision of the project and secured funding. IP and MN are shared-first authors.

Declaration of interest

417   The authors declare no conflicts of interest.

Data and code availability

419   Source data and analysis code are available on Open Science Framework (https://osf.io/cs8d6/), along-
420   side pre-processed eye-tracker data (https://osf.io/mrhk9/. Raw fMRI data is available at the following
421   G-Node Infrastructure repository: https://gin.g-node.org/ipolti/TTC_HPCF.git. The original Bayesian Ob-
422   server Model has been shared by Jazayeri and colleagues and can be found here: https://jazlab.org/
423   resources/.

Methods

Participants

426   The data used in this study were used in a previous report (Polti et al., 2022). Thirty-nine participants
427   (16 women, 23 men, 19-35 years old) were recruited for this study. Five participants were excluded:
428   one was excluded because the eye-tracker calibration failed, one was excluded because they did
429   not follow the task instructions, and three participants were excluded because of technical issues
430   during scanning. A total of 34 participants entered the analysis. The study was approved by the
431   regional committee for medical and health research ethics (project number 2017/969) in Norway
432   and participants gave their written consent prior to scanning in accordance with the Declaration of
433   Helsinki (World Medical Association, 2013).

Task

435   We used a Time-to-contact (TTC) task that required participants to estimate the time when a moving
436   dot reached a target location. Each trial began with the smooth visual pursuit of a dot moving in
437   1 of 24 predefined linear trajectories with 1 of 4 possible speeds: 4.2°/s, 5.8°/s, 7.5°/s and 9.1°/s.
438   All trajectories had two segments, one where the dot was visible ("Gaze trajectory", Fig. 1A; length
439   of 10 dva) and one where the dot was occluded (length of 5 dva). Because all trajectories had the
440   same length, the 4 speeds led to 4 target TTC (t_{TTC}) durations: 1.2s, 0.88s, 0.67s, and 0.55s. A t_{TTC}
441   duration was defined as the time it takes the dot to traverse the occluded segment. When the
442   dot reached the end of the visible segment, a fixation cross remained in place until participants
443   had performed a TTC estimation judgment. The latter consisted of clicking a button when the
444   dot presumably reached the end of the occluded segment ("Boundary", Fig. 1A). After giving a
445   response, participants received visual feedback for 1 s reflecting their TTC estimation accuracy.
446   When accuracy was not high, a visual cue signaled the TTC error direction: either responding too
447   early (underestimation) or too late (overestimation). At the feedback offset, the dot became visible
448   again and remained static for a variable ITI sampled randomly from a uniform distribution ranging
449   from 0.5 to 1.5 s. Then, a new trial began with the dot moving in a different direction. Over the
450   course of 768 trials, we sampled eye movement directions with 15° resolution. Participants were
451   never explicitly informed about the full visual trajectory or the range of t_{TTC}. See previous work of
452   Polti et al. (2022) for more details on the task.

Behavioral analysis

Participants indicated the estimated TTC in each trial via button press. To test if participants discriminated the four target TTCs we used a linear mixed-effect model with estimated TTC (e_{TTC}) as the dependent variable, target TTC (t_{TTC}) as the predictor and separate intercepts and slopes per participant.

We partitioned participants' behavioral performance for each t_{TTC} i using two parameters, Accuracy and Precision (Fig. S1A). $Accuracy_i$ was computed as the absolute difference between the average e_{TTC} ($e\bar{}_{TTC}$) and t_{TTC}, divided by $e\bar{}_{TTC}$:

$$Accuracy_i = \frac{|e\bar{}_{TTC} - t_{TTC}|}{e\bar{}_{TTC}} \tag{1}$$

$Precision_i$ was computed as the coefficient of variation (CV), given by the standard deviation of the e_{TTC} divided by the $e\bar{}_{TTC}$:

$$Precision_i = CV_i = \frac{\sqrt{\sum (e_{TTC} - e\bar{}_{TTC})^2}/N}{e\bar{}_{TTC}} \tag{2}$$

where N is the number of e_{TTC} values. These two parameters can be integrated in a single measurement that reflects the precision-accuracy trade-off when written as a Pythagorean sum, i.e. the root-mean-square error (RMSE):

$$RMSE_i = \sqrt{Precision_i^2 + Accuracy_i^2} \tag{3}$$

In order to analyze the pattern of RMSE across target TTCs, we used a mixed-effect model with RMSE as the dependent variable, target TTC as a quadratic predictor, and separate slopes and intercepts per participant (Fig. 1B). We also ran the same model again while using a linear instead of quadratic trend. We then tested which model best explained the changes in RMSE across target TTCs using a chi-square test.

Imaging data acquisition & preprocessing

Imaging data were acquired on a Siemens 3T MAGNETOM Skyra located at the St. Olavs Hospital in Trondheim, Norway. A T1-weighted structural scan was acquired with 1mm isotropic voxel size. Following EPI-parameters were used: voxel size=2mm isotropic, TR=1020ms, TE=34.6ms, flip angle=55°, multiband factor=6. Participants performed a total of four scanning runs of 16-18 minutes each including a short break in the middle of each run. Functional images were corrected for head motion and co-registered to each individual's structural scan using SPM12 (www.fil.ion.ucl.ac.uk/spm/). We used the FSL topup function to correct field distortions based on one image acquired with inverted phase-encoding direction (https://fsl.fmrib.ox.ac.uk/fsl/fslwiki/topup). Functional images were then spatially normalized to the Montreal Neurological Institute (MNI) brain template and smoothed with a Gaussian kernel with full-width-at-half-maximum of 4 mm for regions-of-interest analysis or with 8 mm for whole-brain analysis. Time series were high-pass filtered with a 128 s cut-off period.

Region-of-interest (ROI) definition and analysis

Rodent studies have consistently reported grid cells in the medial entorhinal cortex (Heys et al., 2014; Moser et al., 2014), which likely corresponds to the posteromedial portion of the entorhinal cortex in humans (Maass et al., 2015; Navarro Schröder et al., 2015). We therefore used a (bilateral) posteromedial entorhinal cortex (pmEC) mask from Navarro Schröder et al. (2015) in all our

fMRI analyses (Fig. S2). As a control region, we chose the early visual cortex (V1) for which, to our knowledge, no hexadirectional signals have been reported. V1 masks were generated for each individual participant based on the automatic parcellation derived from FreeSurfer's structural reconstruction (https://surfer.nmr.mgh.harvard.edu/). A pre-supplementary motor area (preSMA) mask was obtained from the JuBrain SPM anatomy toolbox (https://www.fz-juelich.de/inm/inm-1/EN/Forschung/_docs/SPMAnatomyToolbox/SPMAnatomyToolbox_node.html) in order to post-hoc confirm whether activity observed in voxel-wise analyses corresponded to preSMA. All masks were spatially normalized to the MNI brain template space and re-sliced to the functional imaging resolution using SPM12.

All ROI analyses described in the following were conducted using the following procedure. We extracted beta weights estimated for the respective regressors of interest for all voxels within a region in both hemispheres, averaged them across voxels within that region and performed a one-sample Wilcoxon test on group level against zero as implemented in the software R (https://www.R-project.org).

EC activity as a function of accuracy and as a function of the regression effect

To examine the relationship between behavioral biases and brain activity, we used mass-univariate general linear models (GLM) to model the trial-wise activity of the pmEC voxels as a function of accuracy (i.e. the absolute difference between estimated and target TTC in each trial) and as a function of the regression effect (i.e. the absolute difference between the estimated TTC and the mean of the tested intervals, which was 0.82 s) in the TTC task. To avoid effects of potential colinearity between these regressors, we estimated model weights using two independent GLMs, which modeled the time course of each trial with either one of the two regressors. The GLMs also included one regressor modeling ITIs, one for button presses and one for periods of rest, which were all convolved with the canonical hemodynamic response function in SPM12. In addition, the models included the six realignment parameters obtained during pre-processing as well as a constant term modeling the mean of the time series. After fitting each model, we used the weights estimated for the two regressors to perform ROI analyses for the EC using a two-tailed one-sample Wilcoxon test (Fig. 2).

Hexadirectional analysis of visual grid-like representations

Prior work showed that the MRI signal in the human entorhinal cortex exhibits a six-fold rotationally symmetric modulation as a function of gaze direction, which is thought to reflect grid-cell population activity (Nau et al., 2018b; Julian et al., 2018). Here, we tested whether such grid-like signals were also detectable in our data. The analysis builds on cross-validation to first estimate the putative grid orientation relative to the screen, and then testing in held-out data whether gaze directions aligned to this putative grid orientation are associated with stronger MRI signals than directions misaligned to it.

To estimate the putative grid orientation, we first modeled the activity in each voxel in half of the data using a GLM (odd vs even runs) that incorporated two main regressors of interest. These regressors modeled the sine and cosine of the movement direction of the fixation target θ with a periodicity of 60°, i.e. $\sin(6\theta)$ and $\cos(6\theta)$. For each trial, θ included the tracking and TTC estimation task phases. In addition, nuisance regressors modeled ITIs, the feedback phase, button presses and periods of rest, and two parametric regressors modeled the effect of feedback on the activity during the feedback phase and another one modeling the effect of TTC bias on button presses. All regressors were convolved with the HRF. Because different fixation-target speeds also led to

different TTCs and thus trial durations, and because the amplitude of the HRF-convolved signal scaled with duration, we re-scaled the resulting main regressors to obtain a balanced regressor amplitude for all speeds. Moreover, we added the realignment parameters and a constant term to the model. Each speed level was modeled separately. Weights for all regressors were estimated using SPM12.

We used the beta weights corresponding to the sine ($\beta \sin$) and cosine ($\beta \cos$) of each target TTC level to estimate the putative grid orientation relative to the screen ϕ for voxels within the entorhinal cortex using the following formula: $\phi = \arctan(\beta \sin /\beta \cos)$. The estimated orientations were then circularly averaged across voxels and across runs within each data partition, resulting in a single grid orientation for each target TTC and data partition. We then used the estimated grid orientation in a second GLM to estimate the amplitude of the grid-like signal in its independent data counterpart (Fig. 3A). To do so, we again modeled nuisance variance as described before, this time adding one main regressor per target TTC modeling the cosine of each fixation-target movement direction modulo 60° aligned to the previously estimated mean orientation using the following formula: $\cos(6(\theta - \phi))$. Again, all regressors but the realignment parameters and the constant term were convolved with the HRF, and all main regressors were rescaled to match their amplitude across TTCs. We then again estimated weights for all regressors using SPM12 and averaged them across the pmEC ROI. For each target TTC, we tested its corresponding estimated weight against zero using a one-tailed one-sample Wilcoxon test on group-level (Fig. 3B; Table S1). In order to test for a main effect of target TTC on grid-like signal amplitude, we ran a mixed-effects model with target TTC as predictor, the estimated weights as the dependent variable and participants as the error term. We used two-tailed paired Wilcoxon signed-rank tests to compare differences in grid-like signal between target TTCs (Table S1).

To test whether the grid-like signal found in the pmEC exhibited a specifically 6-fold symmetric periodicity (60°), not other periodicities, we repeated the cross-validation analysis for 4-fold (i.e. 90°, Fig. 3D, Left) and 8-fold (i.e. 45°, Fig. 3D, Center) symmetries. In addition, we tested for 6-fold symmetry in a control region (early visual cortex (V1), Fig. 3D, Right).

In order to exhibit a reliable grid-like signal, a voxel's grid orientation should remain stable over time (i.e. temporal stability). For each participant and target TTC, we therefore computed the percentage of pmEC voxels that maintained an orientation difference of less than 15° between training and test data partitions. We then tested if differences in temporal stability could explain individual differences in the pmEC grid-like modulation for $TTC_{0.86}$ using a Spearman's rank-order correlation (Fig. 3E).

Finally, to asses the behavioral relevance of the pmEC grid-like signal, we ran a linear mixed effect model with the RMSE for all four target TTCs as the dependent variable and their corresponding pmEC grid-like signal as a predictor. The model included separate intercepts and slopes for each participant. We expected that a stronger visual grid-like modulation would predict lower RMSE values (i.e. better performance in the TTC task, Fig. 3F).

Additional analyses of pmEC visual grid-like signals

Besides having high temporal stability, a robust grid-like signal is also expected to have high spatial stability (i.e., pmEC voxel-wise grid orientations should cluster in order to provide a robust mean grid orientation). We used Rayleigh's z-value as a measure of spatial stability: higher z values correspond to higher voxel-wise grid orientation clustering. For each participant and target TTC (t_{TTC}), we computed Rayleigh's test for non-uniformity of circular data on the pmEC voxel-wise grid orien-

576 tations from the training data partition. We tested the Rayleigh's z-values separately for each t_{TTC}
577 against zero using one-tailed one-sample Wilcoxon tests on group-level. In order to compare spa-
578 tial stability between t_{TTC}, we again used a mixed-effects model incorporating spatial stability as a
579 dependent variable, t_{TTC} as a predictor, and participants as the error term (Fig. S3B). We further
580 used a Spearman's rank-order correlation to test if individual differences in spatial stability could
581 predict the cross-validated grid-like signal amplitude estimated for $TTC_{0.86}$ (Fig. S3C; Spearman's
582 *rho = 0.49, p = 0.003*).

583 Differences in grid-like signal amplitude across t_{TTC} could also be explained by differences in tem-
584 poral stability. We thus used a mixed-effects model with temporal stability as a dependent variable,
585 t_{TTC} as a predictor and participants as the error term to test this possibility (Fig. S3A). This analysis
586 was conducted both for the pmEC and the early visual cortex control (Fig. S3D).

Bayesian observer model

588 The Bayesian observer model, developed originally by Jazayeri and colleagues (Jazayeri, Shadlen,
589 2010), has been successfully adapted and applied several times to model timing behavior (Jazayeri,
590 Shadlen, 2015; Remington et al., 2018; Chang, Jazayeri, 2018; De Kock et al., 2021). We adapted the
591 original code provided at https://jazlab.org/resources/ in order to model participants' behavior in our
592 TTC estimation task.

593 The Bayesian observer model is composed of three stages. In the first stage, the observer makes
594 a noisy duration measurement (m_{vt}) of the visual tracking period (VT, Fig. 1A), from the movement
595 onset of the fixation disc until it becomes occluded. Measurement noise was modeled as a zero-
596 mean scalar Gaussian likelihood distribution (Gibbon, 1977). Specifically, the standard deviation of
597 measurement noise was scaled as a function of the VT duration with constant of proportionality
598 w_m (Weber fraction for VT duration measurement).

599 During the second stage, the Bayesian observer integrates two sources of information to minimize
600 their mismatch: the likelihood of m_{vt} and a prediction based on prior knowledge (a statistical rep-
601 resentation of the temporal context, i.e., the distribution of sampled VT durations). The prior was
602 modeled as a Gaussian distribution centered on the mean of the range of sampled VT durations,
603 with standard deviation equal to the standard deviation of the sampled VT durations. As a result of
604 Bayesian integration, the posterior distribution is then computed over the sampled VT durations.

605 In the third stage, the Bayesian observer selects the optimal VT duration estimate corresponding
606 to the mean of the posterior based on a quadratic loss function. This value is further scaled by 0.5,
607 a gain factor (Gf) equal to the ratio of distances between the occluded and visible segments of the
608 path (5 / 10 dva; Fig. 1A). The scaled value corresponds to the optimal estimated TTC (e_{TTC}), which
609 is then augmented by TTC production noise to account for motor variability. TTC production noise
610 was modeled as a scalar Gaussian distribution centered at the mean of the posterior. The standard
611 deviation of TTC production noise scaled as a function of e_{TTC} with constant of proportionality w_p
612 (Weber fraction for TTC production). To account for idiosyncratic response biases (e.g. consistently
613 producing TTC responses earlier or later than expected), the model includes an offset parameter
614 o_b (Remington et al., 2018).

615 In order to fit the Bayesian observer model to behavioral data, we used a cross-validation proce-
616 dure. We first split the data of each participant into two independent halves (384 trials each) with
617 an equal number of trials for each t_{TTC}. The trials were randomly sampled without replacement
618 throughout the experimental session. The model parameters (w_m, w_p, o_b) were fitted separately on
619 each data partition by maximizing the log-likelihood of participants' responses given the sampled

TTCs using the $fminsearch$ MATLAB function. Parameter searches were repeated 10 times using different initialization values, showing a high degree of consistency between iterations and data partitions (Fig. S4A). Given such consistency, we used as final model parameters the median value across all the fits to the data (Fig. S4B). These model parameters were further used for model simulations, where we generated the same number of trials and t_{TTC} combinations as participants had in each data partition.

To evaluate the model predictions we computed the RMSE of each t_{TTC} as a summary statistic and calculated the Mean Absolute Error (MAE) between the observed and predicted RMSE (Fig. 4B). To corroborate that the model replicated participants' quadratic RMSE pattern across t_{TTC}, we ran a mixed-effects model with the model RMSE as a dependent variable, target TTC as a quadratic predictor and separate intercepts and slopes per participant. Furthermore, to test the model suitability to replicate the observed relationship between pmEC grid-like signals and RMSE, we used a mixed-effects model with model RMSE as the dependent variable, participants' pmEC grid-like signal as a predictor, and separate intercepts and slopes per participant.

In our model, we assumed a prior Gaussian distribution centered on the mean of the sampled VT durations (1.64 s), and Gaussian likelihood functions centered on the respective value of each sampled VT duration (1.1 s, 1.34 s, 1.72 s and 2.4 s; Fig. 4A, Left). With these settings, the smallest mismatch between prior and likelihood occurs for the sampled VT duration 1.72 s (Fig. 4A, Left, yellow lines). Consequently, the lowest RMSE values are observed at the corresponding t_{TTC} of this VT duration (0.86 s; Fig. 4A, Center). We explored alternative configurations by running model simulations where the prior was centered close to a different VT duration each time. The different prior values were obtained by multiplying each VT duration with the ratio between the average VT duration 1.64 s and the VT duration 1.72 s. When scaled by Gf the prior means correspond to 0.52 s, 0.64 s, 0.82 s and 1.14 s, and the sampled VT durations correspond to the t_{TTC} 0.55 s, 0.67 s, 0.86 s and 1.2 s (Fig. S4D). For each participant and model, we simulated the same number of trials as were originally tested and calculated the MAE between the observed and simulated RMSE (Fig. S4C). To examine potential differences in MAE across model simulations with different prior means, we ran a mixed-effects model with MAE as the dependent variable, prior mean value as predictor and participants as the error term. We found a main effect of prior mean on the MAE ($;$ $F(3) = 44.23, p = 2.2x10^{-16}, \epsilon^2 = 0.55, CI : [0.44, 1]$). We expected the model with the prior centered on the mean interval to show the lowest MAE. To test this prediction, we conducted one-tailed paired Wilcoxon signed-rank tests between each model pair (Table S5).

Eye tracking

We used an MR-compatible infrared eye tracker with long-range optics (Eyelink 1000) to monitor gaze position at a rate of 500 hz during the experiment. After blink removal, the eye tracking data was linearly detrended, median centered, downsampled to the screen refresh rate of 120 hz and smoothed with a running-average kernel of 100 ms. Fixation error was computed separately for each participant and trial as the euclidean distance between the fixation target and the measured gaze position. In order to test for systematic imbalances or biases in viewing behavior, we used separate mixed-effects models (one per t_{TTC}) with fixation error as the dependent variable, direction as predictor, and participants as the error term. There were no significant differences in fixation error across directions (Fig. S1B; Table S6).

References

Acerbi Luigi, Wolpert Daniel M., Vijayakumar Sethu. Internal Representations of Temporal Statistics and Feedback Calibrate Motor-Sensory Interval Timing // PLoS Computational Biology. 2012. 8, 11. e1002771.

Ambrogioni Luca, Ólafsdóttir H. Freyja. Rethinking the hippocampal cognitive map as a meta-learning computational module // Trends in Cognitive Sciences. 2023. 27, 8. 702–712.

Aronov Dmitriy, Nevers Rhino, Tank David W. Mapping of a non-spatial dimension by the hippocampal–entorhinal circuit // Nature. 2017. 543, 7647. 719–722.

Banino Andrea, Barry Caswell, Uria Benigno, Blundell Charles, Lillicrap Timothy, Mirowski Piotr, Pritzel Alexander, Chadwick Martin J., Degris Thomas, Modayil Joseph, Wayne Greg, Soyer Hubert, Viola Fabio, Zhang Brian, Goroshin Ross, Rabinowitz Neil, Pascanu Razvan, Beattie Charlie, Petersen Stig, Sadik Amir, Gaffney Stephen, King Helen, Kavukcuoglu Koray, Hassabis Demis, Hadsell Raia, Kumaran Dharshan. Vector-based navigation using grid-like representations in artificial agents // Nature. 2018. 557, 7705. 429–433.

Bao Xiaojun, Gjorgieva Eva, Shanahan Laura K., Howard James D., Kahnt Thorsten, Gottfried Jay A. Grid-like Neural Representations Support Olfactory Navigation of a Two-Dimensional Odor Space // Neuron. 2019. 102, 5. 1066–1075.e5.

Barry Caswell, Ginzberg Lin Lin, O'Keefe John, Burgess Neil. Grid cell firing patterns signal environmental novelty by expansion // Proceedings of the National Academy of Sciences of the United States of America. X 2012. 109, 43. 17687–17692.

Barry Caswell, Hayman Robin, Burgess Neil, Jeffery Kathryn J. Experience-dependent rescaling of entorhinal grids // Nature Neuroscience. VI 2007. 10, 6. 682–684. Number: 6 Publisher: Nature Publishing Group.

Behrens Timothy E.J., Muller Timothy H., Whittington James C.R., Mark Shirley, Baram Alon B., Stachenfeld Kimberly L., Kurth-Nelson Zeb. What Is a Cognitive Map? Organizing Knowledge for Flexible Behavior // Neuron. 2018. 100, 2. 490–509.

Bellmund Jacob, Gärdenfors Peter, Moser Edvard I., Doeller Christian F. Navigating cognition: Spatial codes for human thinking // Science. 2018. 362, 6415. eaat6766.

Bellmund Jacob, Polti Ignacio, Doeller Christian F. Sequence memory in the hippocampal–entorhinal region // Journal of Cognitive Neuroscience. 2020a. 32, 11. 2056–2070.

Bellmund Jacob L. S., Cothi William de, Ruiter Tom A., Nau Matthias, Barry Caswell, Doeller Christian F. Deforming the metric of cognitive maps distorts memory // Nature Human Behaviour. 2020b. 4, 2. 177–188.

Bellmund Jacob L. S., Deuker Lorena, Montijn Nicole D., Doeller Christian F. Mnemonic construction and representation of temporal structure in the hippocampal formation // Nature Communications. 2022. 13, 1. 3395.

Bicanski Andrej, Burgess Neil. Neuronal vector coding in spatial cognition // Nature Reviews Neuroscience. 2020. 21, 9. 453–470.

Bigus Erin R., Lee Hyun-Woo, Shi Jiani, Heys James G. Medial entorhinal cortex plays a specialized role in learning of flexible, context-dependent interval timing behavior. I 2023.

Boccara Charlotte N., Nardin Michele, Stella Federico, O'Neill Joseph, Csicsvari Jozsef. The entorhinal cognitive map is attracted to goals // Science. 2019. 363, 6434. 1443–1447.

Bousquet Olivier, Balakrishnan Karthik, Honavar Vasant. Is the Hippocampus a Kalman Filter? // Pacific Symposium on Biocomputing. 1998. 657–668.

Buckmaster Cindy A., Eichenbaum Howard, Amaral David G., Suzuki Wendy A., Rapp Peter R. Entorhinal Cortex Lesions Disrupt the Relational Organization of Memory in Monkeys // Journal of Neuroscience. XI 2004. 24, 44. 9811–9825. Publisher: Society for Neuroscience Section: Behavioral/Systems/Cognitive.

Bush Daniel, Barry Caswell, Manson Daniel, Burgess Neil. Using Grid Cells for Navigation // Neuron. 2015. 87, 3. 507–520.

Butler William N., Hardcastle Kiah, Giocomo Lisa M. Remembered reward locations restructure entorhinal spatial maps // Science. 2019. 363, 6434. 1447–1452.

Chang Chia Jung, Jazayeri Mehrdad. Integration of speed and time for estimating time to contact // Proceedings of the National Academy of Sciences of the United States of America. 2018. 115, 12. E2879–E2887.

Chen Xiaoli, He Qiliang, Kelly Jonathan W., Fiete Ila R., McNamara Timothy P. Bias in Human Path Integration Is Predicted by Properties of Grid Cells // Current biology: CB. 2015. 25, 13. 1771–1776.

Cheng Ken, Shettleworth Sara J., Huttenlocher Janellen, Rieser John J. Bayesian integration of spatial information // Psychological Bulletin. 2007. 133, 4. 625–637.
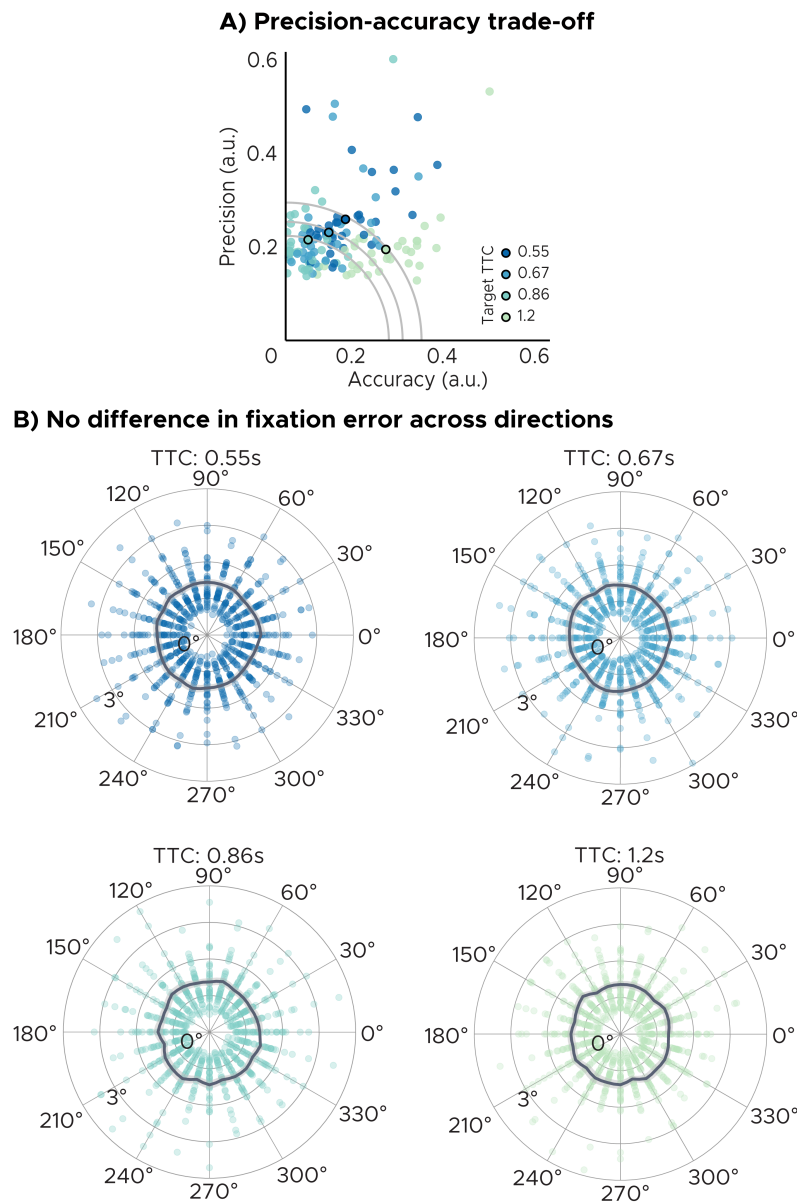
Cicchini Guido Marco, Arrighi Roberto, Cecchetti Luca, Giusti Marco, Burr David C. Optimal Encoding of Interval Timing in Expert Percussionists // Journal of Neuroscience. 2012. 32, 3. 1056–1060.

Clark Andy. Whatever next? Predictive brains, situated agents, and the future of cognitive science // Behavioral and Brain Sciences. 2013. 36, 3. 181–204.

Constantinescu Alexandra O., O'Reilly Jill X., Behrens Timothy E. J. Organizing conceptual knowledge in humans with a gridlike code // Science. 2016. 352, 6292. 1464–1468.

Cothi William de, Nyberg Nils, Griesbauer Eva-Maria, Ghanamé Carole, Zisch Fiona, Lefort Julie M., Fletcher Lydia, Newton Coco, Renaudineau Sophie, Bendor Daniel, Grieves Roddy, Duvelle Éléonore, Barry Caswell, Spiers Hugo J. Predictive maps in rats and humans for spatial navigation // Current Biology. 2022. 32, 17. 3676–3689.e5.

Dayan Peter, Daw Nathaniel D. Decision theory, reinforcement learning, and the brain // Cognitive, Affective, & Behavioral Neuroscience. 2008. 8, 4. 429–453.

De Kock Rose, Zhou Weiwei, Joiner Wilsaan M, Wiener Martin. Slowing the body slows down time perception // eLife. IV 2021. 10. e63607. Publisher: eLife Sciences Publications, Ltd.

Dias Marcelo, Ferreira Raquel, Remondes Miguel. Medial Entorhinal Cortex Excitatory Neurons Are Necessary for Accurate Timing // Journal of Neuroscience. XII 2021. 41, 48. 9932–9943.

Doeller Christian F., Barry Caswell, Burgess Neil. Evidence for grid cells in a human memory network // Nature. 2010. 463, 7281. 657–661.

Doeller Christian F., King John A., Burgess Neil. Parallel striatal and hippocampal systems for landmarks and boundaries in spatial memory // Proceedings of the National Academy of Sciences. 2008. 105, 15. 5915–5920.

Eichenbaum Howard, Dudchenko Paul, Wood Emma, Shapiro Matthew, Tanila Heikki. The Hippocampus, Memory, and Place Cells: Is It Spatial Memory or a Memory Space? // Neuron. 1999. 23, 2. 209–226.

Epstein Russell A., Patai Eva Zita, Julian Joshua B., Spiers Hugo J. The cognitive map in humans: spatial navigation and beyond // Nature Neuroscience. 2017. 20, 11. 1504–1513.

Fernández Guillén, Brewer James B., Zhao Zuo, Glover Gary H., Gabrieli John D.E. Level of sustained entorhinal activity at study correlates with subsequent cued-recall performance: A functional magnetic resonance imaging study with high acquisition rate // Hippocampus. 1999. 9, 1. 35–44.

Fiser József, Berkes Pietro, Orbán Gergő, Lengyel Máté. Statistically optimal perception and learning: from behavior to neural representations // Trends in Cognitive Sciences. 2010. 14, 3. 119–130.

Fortin Norbert J., Agster Kara L., Eichenbaum Howard B. Critical role of the hippocampus in memory for sequences of events // Nature Neuroscience. 2002. 5, 5. 458–462.

Friston Karl, Buzsáki Gyorgy. The Functional Anatomy of Time: What and When in the Brain // Trends in Cognitive Sciences. 2016. 20, 7. 500–511.

Fuhs Mark C., Touretzky David S. Context Learning in the Rodent Hippocampus // Neural Computation. 2007. 19, 12. 3173–3215.

Garvert Mona M, Dolan Raymond J, Behrens Timothy EJ. A map of abstract relational knowledge in the human hippocampal–entorhinal cortex // eLife. 2017. 6. e17086.

Geerts Jesse P., Chersi Fabian, Stachenfeld Kimberly L., Burgess Neil. A general model of hippocampal and dorsal striatal learning and decision making // Proceedings of the National Academy of Sciences. 2020. 117, 49. 31427–31437.

Gibbon John. Scalar expectancy theory and Weber's law in animal timing // Psychological Review. 1977. 84, 3. 279–325.

Hafting Torkel, Fyhn Marianne, Molden Sturla, Moser May-Britt, Moser Edvard I. Microstructure of a spatial map in the entorhinal cortex // Nature. 2005. 436, 7052. 801–806.

Hardcastle Kiah, Ganguli Surya, Giocomo Lisa M. Environmental Boundaries as an Error Correction Mechanism for Grid Cells // Neuron. V 2015. 86, 3. 827–839.

Hargreaves Eric L., Mattfeld Aaron T., Stark Craig E. L., Suzuki Wendy A. Conserved fMRI and LFP Signals during New Associative Learning in the Human and Macaque Monkey Medial Temporal Lobe // Neuron. 2012. 74, 4. 743–752.

Hartley Tom, Trinkler Iris, Burgess Neil. Geometric determinants of human spatial memory // Cognition. 2004. 94, 1. 39–75.

Heald James B., Wolpert Daniel M., Lengyel Máté. The Computational and Neural Bases of Context-Dependent Learning // Annual Review of Neuroscience. 2023. 46, 1. 233–258.

760 *Henke Josephine, Bunk David, Werder Dina von, Häusler Stefan, Flanagin Virginia L, Thurley Kay*. Distributed coding of
761   duration in rodent prefrontal cortex during time reproduction // eLife. XII 2021. 10. e71612. Publisher: eLife
762   Sciences Publications, Ltd.

763 *Heys James G., Dombeck Daniel A.* Evidence for a subcircuit in medial entorhinal cortex representing elapsed time
764   during immobility // Nature Neuroscience. 2018. 21, 11. 1574–1582.

765 *Heys James G., Rangarajan Krsna V., Dombeck Daniel A.* The Functional Micro-organization of Grid Cells Revealed by
766   Cellular-Resolution Imaging // Neuron. 2014. 84, 5. 1079–1090.

767 *Heys James G., Wu Zihan, Allegra Mascaro Anna Letizia, Dombeck Daniel A.* Inactivation of the Medial Entorhinal Cortex
768   Selectively Disrupts Learning of Interval Timing // Cell Reports. 2020. 32, 12. 108163.

769 *Hsieh Liang-Tien, Gruber Matthias J., Jenkins Lucas J., Ranganath Charan*. Hippocampal activity patterns carry information
770   about objects in temporal context // Neuron. 2014. 81, 5. 1165–1178.

771 *Jazayeri Mehrdad, Shadlen Michael N.* Temporal context calibrates interval timing // Nature Neuroscience. 2010. 13, 8.
772   1020–1026.

773 *Jazayeri Mehrdad, Shadlen Michael N.* A Neural Mechanism for Sensing and Reproducing a Time Interval // Current
774   Biology. X 2015. 25, 20. 2599–2609.

775 *Julian Joshua B., Doeller Christian F.* Remapping and realignment in the human hippocampal formation predict context-
776   dependent spatial behavior // Nature Neuroscience. VI 2021. 24, 6. 863–872.

777 *Julian Joshua B., Keinath Alexandra T., Frazzetta Giulia, Epstein Russell A.* Human entorhinal cortex represents visual
778   space using a boundary-anchored grid // Nature Neuroscience. II 2018. 21, 2. 191–194.

779 *Kang Yul Hr, Wolpert Daniel M., Lengyel Máté*. Spatial uncertainty and environmental geometry in navigation // bioRxiv:
780   The Preprint Server for Biology. 2023. 2023.01.30.526278.

781 *Keinath Alexandra T, Epstein Russell A, Balasubramanian Vijay*. Environmental deformations dynamically shift the grid
782   cell spatial metric // eLife. 2018. 7. e38169. Publisher: eLife Sciences Publications, Ltd.

783 *Keinath Alexandra T., Rechnitz Ohad, Balasubramanian Vijay, Epstein Russell A.* Environmental deformations dynamically
784   shift human spatial memory // Hippocampus. 2021. 31, 1. 89–101.

785 *Kessler Fabian, Frankenstein Julia, Rothkopf Constantin A.* A Dynamic Bayesian Actor Model explains Endpoint Variability
786   in Homing Tasks. 2022.

787 *Killian Nathaniel J., Jutras Michael J., Buffalo Elizabeth a.* A map of visual space in the primate entorhinal cortex // Nature.
788   2012. 491, 7426. 761–764.

789 *Krupic Julija, Bauza Marius, Burton Stephen, Barry Caswell, O'Keefe John*. Grid cell symmetry is shaped by environmental
790   geometry // Nature. II 2015. 518, 7538. 232–235. Number: 7538 Publisher: Nature Publishing Group.

791 *Kunz Lukas, Maidenbaum Shachar, Chen Dong, Wang Liang, Jacobs Joshua, Axmacher Nikolai*. Mesoscopic Neural Repre-
792   sentations in Spatial Navigation // Trends in Cognitive Sciences. 2019. 23, 7. 615–630.

793 *Kunz Lukas, Schröder Tobias Navarro, Lee Hweeling, Montag Christian, Lachmann Bernd, Sariyska Rayna, Reuter Martin,*
794   *Stirnberg Rüdiger, Stöcker Tony, Messing-Floeter Paul Christian, Fell Juergen, Doeller Christian F., Axmacher Nikolai*. Re-
795   duced grid-cell–like representations in adults at genetic risk for Alzheimer's disease // Science. 2015. 350, 6259.
796   430–433. Publisher: American Association for the Advancement of Science.

797 *Körding Konrad P., Wolpert Daniel M.* Bayesian integration in sensorimotor learning // Nature. 2004. 427, 6971. 244–
798   247.

799 *Lisman John, Redish A.d.* Prediction, sequences and the hippocampus // Philosophical Transactions of the Royal Society
800   B: Biological Sciences. 2009. 364, 1521. 1193–1201. Publisher: Royal Society.

801 *Maass Anne, Berron David, Libby Laura A, Ranganath Charan, Düzel Emrah*. Functional subregions of the human entorhi-
802   nal cortex // eLife. 2015. 4. e06426. Publisher: eLife Sciences Publications, Ltd.

803 *Manns Joseph R., Eichenbaum Howard*. Evolution of declarative memory // Hippocampus. 2006. 16, 9. 795–808.

804 *Meirhaeghe Nicolas, Sohn Hansem, Jazayeri Mehrdad*. A precise and adaptive neural mechanism for predictive temporal
805   processing in the frontal cortex // Neuron. 2021. 109, 18. 2995–3011.e5.

806 *Miyazaki Makoto, Nozaki Daichi, Nakajima Yasoichi*. Testing Bayesian Models of Human Coincidence Timing // Journal
807   of Neurophysiology. 2005. 94, 1. 395–399. Publisher: American Physiological Society.

Momennejad I., Russek E. M., Cheong J. H., Botvinick M. M., Daw N. D., Gershman S. J. The successor representation in human reinforcement learning // Nature Human Behaviour. 2017. 1, 9. 680–692.

Montchal Maria E., Reagh Zachariah M., Yassa Michael A. Precise temporal memories are supported by the lateral entorhinal cortex in humans // Nature Neuroscience. 2019. 22, 2. 284–288.

Moser Edvard I., Roudi Yasser, Witter Menno P., Kentros Clifford, Bonhoeffer Tobias, Moser May-Britt. Grid cells and cortical representation // Nature Reviews Neuroscience. 2014. 15, 7.

Nau Matthias, Julian Joshua B., Doeller Christian F. How the Brain's Navigation System Shapes Our Visual Experience // Trends in Cognitive Sciences. 2018a. 22, 9. 810–825.

Nau Matthias, Navarro Schröder Tobias, Bellmund Jacob L. S., Doeller Christian F. Hexadirectional coding of visual space in human entorhinal cortex // Nature Neuroscience. 2018b. 21, 2. 188–190.

Navarro Schröder Tobias, Haak Koen V, Zaragoza Jimenez Nestor I, Beckmann Christian F, Doeller Christian F. Functional topography of the human entorhinal cortex // eLife. VI 2015. 4. e06738. Publisher: eLife Sciences Publications, Ltd.

Nitsch Alexander, Garvert Mona M., Bellmund Jacob L. S., Schuck Nicolas W., Doeller Christian F. Grid-like entorhinal representation of an abstract value space during prospective decision making. 2023.

Niv Yael. Reinforcement learning in the brain // Journal of Mathematical Psychology. Special Issue: Dynamic Decision Making. 2009. 53, 3. 139–154.

O'Keefe J., Nadel L. The Hippocampus as a Cognitive Map. Oxford, UK: Oxford University Press, 1978.

Park Seongmin A., Miller Douglas S., Boorman Erie D. Inferences on a multidimensional social hierarchy use a grid-like code // Nature Neuroscience. 2021. 24, 9. 1292–1301.

Penny Will D., Zeidman Peter, Burgess Neil. Forward and Backward Inference in Spatial Cognition // PLOS Computational Biology. 2013. 9, 12. e1003383.

Petzschner Frederike H., Glasauer Stefan. Iterative Bayesian Estimation as an Explanation for Range and Regression Effects: A Study on Human Path Integration // Journal of Neuroscience. 2011. 31, 47. 17220–17229.

Petzschner Frederike H., Glasauer Stefan, Stephan Klaas E. A Bayesian perspective on magnitude estimation // Trends in Cognitive Sciences. 2015. 19, 5. 285–293.

Pezzulo Giovanni, Kemere Caleb, Meer Matthijs A.A. van der. Internally generated hippocampal sequences as a vantage point to probe future-oriented cognition // Annals of the New York Academy of Sciences. 2017. 1396, 1. 144–165.

Polti Ignacio, Nau Matthias, Kaplan Raphael, Wassenhove Virginie van, Doeller Christian F. Rapid encoding of task regularities in the human hippocampus guides sensorimotor timing // eLife. 2022. 11. e79027.

Remington Evan D., Parks Tiffany V., Jazayeri Mehrdad. Late Bayesian inference in mental transformations // Nature Communications. X 2018. 9, 1. 4419.

Rolando Felipe, Kononowicz Tadeusz W., Duhamel Jean-René, Doyère Valérie, Wirth Sylvia. Distinct neural adaptations to time demand in the striatum and the hippocampus // Current biology: CB. 2024. 34, 1. 156–170.e7.

Schapiro A., Turk-Browne N. Statistical Learning // Brain Mapping. 2015. 501–506.

Schapiro Anna C., Kustner Lauren V., Turk-Browne Nicholas B. Shaping of Object Representations in the Human Medial Temporal Lobe Based on Temporal Regularities // Current Biology. 2012. 22, 17. 1622–1627.

Schapiro Anna C., Turk-Browne Nicholas B., Norman Kenneth A., Botvinick Matthew M. Statistical learning of temporal community structure in the hippocampus // Hippocampus. 2016. 26, 1. 3–8.

Schiller Daniela, Eichenbaum Howard, Buffalo Elizabeth A., Davachi Lila, Foster David J., Leutgeb Stefan, Ranganath Charan. Memory and space: Towards an understanding of the cognitive map // Journal of Neuroscience. 2015. 35, 41. 13904–13911.

Sohn Hansem, Narain Devika, Meirhaeghe Nicolas, Jazayeri Mehrdad. Bayesian Computation through Cortical Latent Dynamics // Neuron. IX 2019. 103, 5. 934–947.e5.

Stachenfeld Kimberly L., Botvinick Matthew M., Gershman Samuel J. The hippocampus as a predictive map // Nature Neuroscience. XI 2017. 20, 11. 1643–1653.

Stangl Matthias, Achtzehn Johannes, Huber Karin, Dietrich Caroline, Tempelmann Claus, Wolbers Thomas. Compromised Grid-Cell-like Representations in Old Age as a Key Mechanism to Explain Age-Related Navigational Deficits // Current Biology. 2018. 28, 7. 1108–1115.e6.

Staresina Bernhard P., Alink Arjen, Kriegeskorte Nikolaus, Henson Richard N. Awake reactivation predicts memory in humans // Proceedings of the National Academy of Sciences. 2013. 110, 52. 21159–21164.

Staudigl Tobias, Leszczynski Marcin, Jacobs Joshua, Sheth Sameer A., Schroeder Charles E., Jensen Ole, Doeller Christian F. Hexadirectional Modulation of High-Frequency Electrophysiological Activity in the Human Anterior Medial Temporal Lobe Maps Visual Space // Current Biology. X 2018. 28, 20. 3325–3329.e4.

Syversen Ingrid Framås, Witter Menno P., Kobro-Flatmoen Asgeir, Goa Pål Erik, Navarro Schröder Tobias, Doeller Christian F. Structural connectivity-based segmentation of the human entorhinal cortex // NeuroImage. 2021. 245. 118723.

Theves Stephanie, Fernandez Guillén, Doeller Christian F. The Hippocampus Encodes Distances in Multidimensional Feature Space // Current Biology. 2019. 29, 7. 1226–1231.e3.

Theves Stephanie, Fernández Guillén, Doeller Christian F. The Hippocampus Maps Concept Space, Not Feature Space // Journal of Neuroscience. 2020. 40, 38. 7318–7325.

Vetter Philipp, Wolpert Daniel M. Context Estimation for Sensorimotor Control // Journal of Neurophysiology. 2000. 84, 2. 1026–1034.

Viganò Simone, Bayramova Rena, Doeller Christian F., Bottini Roberto. Mental search of concepts is supported by egocentric vector representations and restructured grid maps // Nature Communications. 2023. 14, 1. 8132.

Viganò Simone, Piazza Manuela. Distance and Direction Codes Underlie Navigation of a Novel Semantic Space in the Human Brain // Journal of Neuroscience. 2020. 40, 13. 2727–2736.

Viganò Simone, Rubino Valerio, Soccio Antonio Di, Buiatti Marco, Piazza Manuela. Grid-like and distance codes for representing word meaning in the human brain // NeuroImage. 2021. 232. 117876.

Vo Annette, Tabrizi Nina S., Hunt Thomas, Cayanan Kayla, Chitale Saee, Anderson Lucy G., Tenney Sarah, White André O., Sabariego Marta, Hales Jena B. Medial entorhinal cortex lesions produce delay-dependent disruptions in memory for elapsed time // Neurobiology of Learning and Memory. 2021. 185. 107507.

Wagner Isabella C., Graichen Luise P., Todorova Boryana, Lüttig Andre, Omer David B., Stangl Matthias, Lamm Claus. Entorhinal grid-like codes and time-locked network dynamics track others navigating through space // Nature Communications. 2023. 14, 1. 231.

Wang Jing, Narain Devika, Hosseini Eghbal A., Jazayeri Mehrdad. Flexible timing by temporal scaling of cortical responses // Nature Neuroscience. I 2018. 21, 1. 102–110. Number: 1 Publisher: Nature Publishing Group.

Whittington James C. R., Muller Timothy H., Mark Shirley, Chen Guifen, Barry Caswell, Burgess Neil, Behrens Timothy E. J. The Tolman-Eichenbaum Machine: Unifying Space and Relational Memory through Generalization in the Hippocampal Formation // Cell. XI 2020. 183, 5. 1249–1263.e23.

Wiener Martin, Michaelis Kelly, Thompson James C. Functional correlates of likelihood and prior representations in a virtual distance task // Human Brain Mapping. 2016. 37, 9. 3172–3187.

Witter Menno P., Amaral David G. CHAPTER 21 - Hippocampal Formation // The Rat Nervous System (Third Edition). Burlington: Academic Press, I 2004. 635–704.

World Medical Association . World Medical Association Declaration of Helsinki: Ethical Principles for Medical Research Involving Human Subjects // JAMA. 2013. 310, 20. 2191–2194.

Supplementary Material

Figure S1: A) Precision (Coefficient of Variation) as a function of Accuracy (the absolute difference between average estimated TTC and target TTC, normalized by the average estimated TTC) separately for each target TTC. The distance from the origin is the TTC performance, i.e. the Root-Mean-Square-Error (RMSE). Solid grey quarter circle lines represent the locus of the mean RMSE for each target TTC. The same RMSE can arise from low accuracy and high precision, and from high accuracy and low precision. Mean RMSE for each target TTC represented by a colored dot with a black edge. Target TTCs are color coded. B) Euclidean distance between fixation target and gaze (fixation error). There were no significant differences in fixation error across all 24 gaze directions. Fixation quality does not affect the gaze-dependent hexadirectional modulation in EC presented in this study. Each dot per direction represents a single participant. Target TTCs are color coded. Group-level mean (black line) and SEM (gray shade). Fixation error displayed as degree of visual angle (radial axis). AB) Single-participant data plotted as dots.

Regions of interest

Figure S2: Regions of interest (ROIs). Red) posterior medial entorhinal cortex (pmEC) ROI representing the human homolog of rodent medial entorhinal cortex. This mask was obtained from Navarro Schröder et al. (2015). Green) pre-supplementary motor area (preSMA) obtained from the JuBrain SPM anatomy toolbox. Blue) early visual cortex (V1) anatomically defined for each participant using FreeSurfer's cortical parcellation. ROIs superimposed onto a 2mm resolution skull-stripped structural template brain. MNI coordinates added.
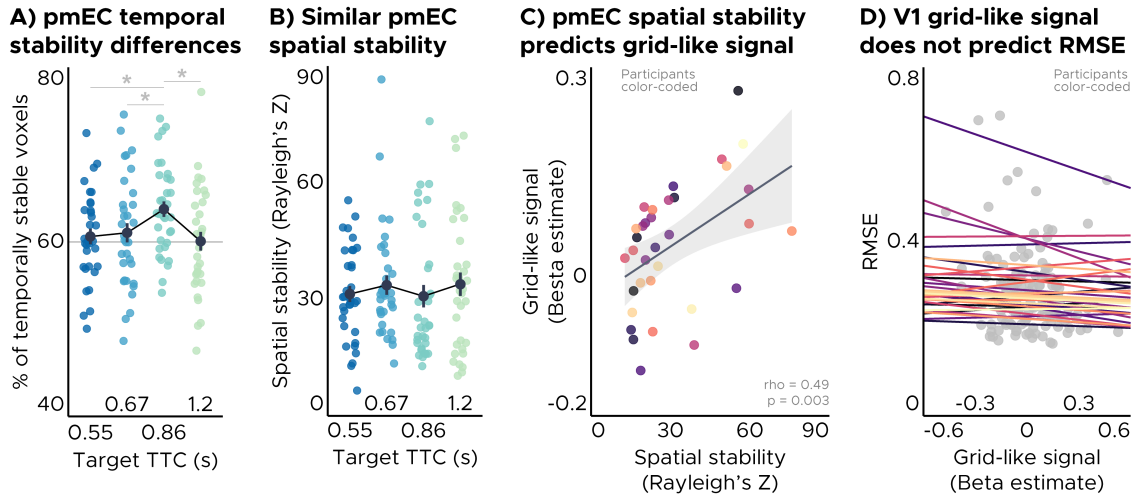
Figure S3: Additional pmEC grid-like signal analyses. A) Significant differences in temporal stability of grid-like signals in pmEC voxels across target TTCs. $TTC_{0.86}$ showed the highest percent of pmEC temporally stable voxels. B) No significant difference in spatial stability of grid-like signals in pmEC voxels across target TTCs. C) $TTC_{0.86}$ pmEC spatial stability predicts corresponding grid-like signal across participants. Each dot represents a single participant. Regression line (black) and standard error (gray shade). D) Within-participant V1 grid-like signal does not predict TTC estimation RMSE. Separate regression lines are plotted for each participant. AB) Depicted are the mean and SEM across participants (black dot and line) overlaid on single participant data (colored dots). Target TTCs are color coded. CD) Participants are color-coded.

Figure S4: Bayesian observer model parameters and simulations. A) Model parameter differences across data partitions. Distribution of differences in parameter value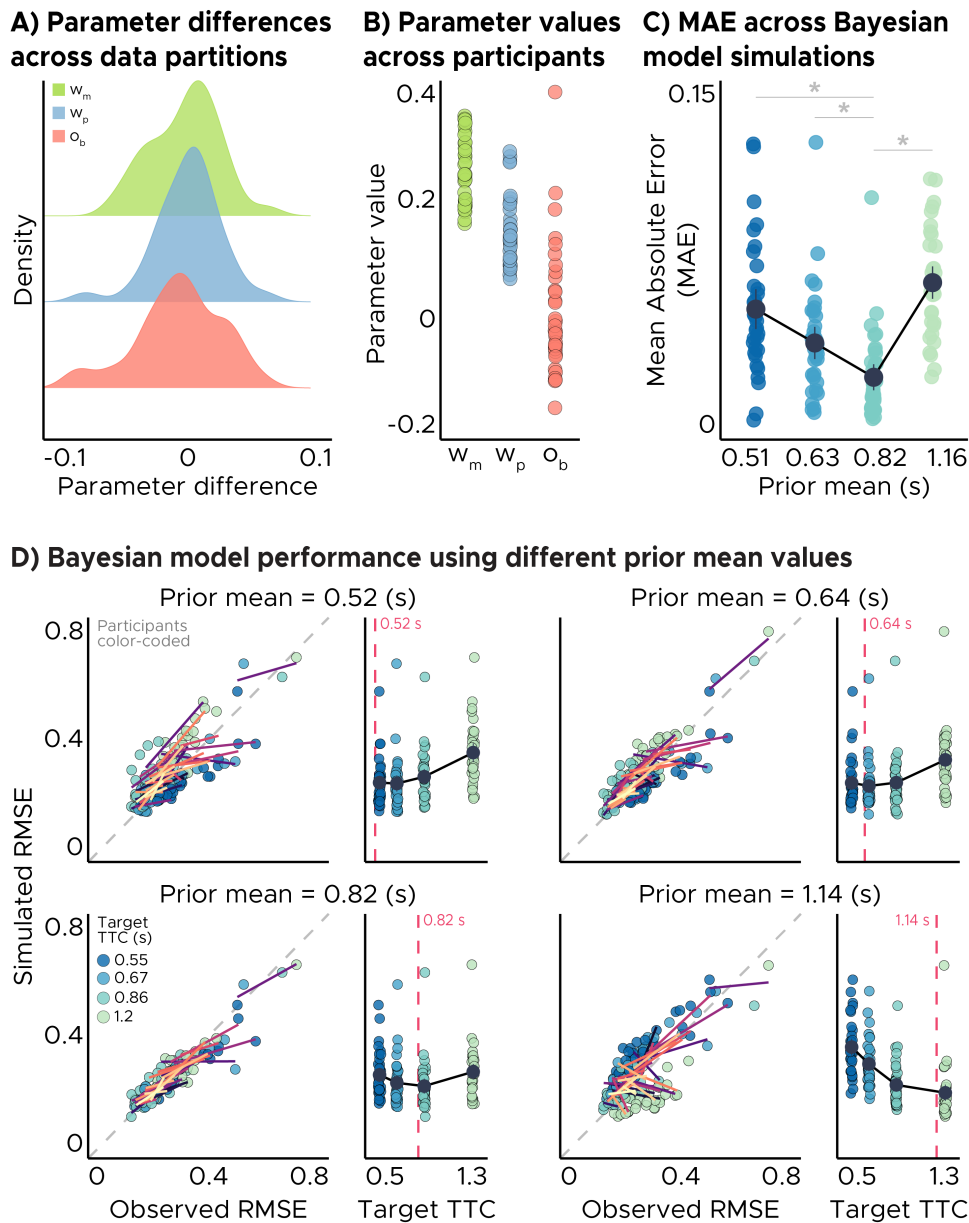s across data partitions centered around zero across participants. The magnitude of these differences were relatively small. Model parameters: w_m (measurement noise parameter, green), w_p (TTC production noise, blue), o_b (response bias, red). **B)** Median parameter value across data partitions for each participant. Parameter values showed differences across participants. Parameters were color coded. **C)** Mean Absolute Error (MAE) across Bayesian model simulations with different prior mean values. Group average model performance was best for simulations that set the prior mean value at 0.82 s, the average across sampled durations. Model simulations with different prior mean values were color coded. Statistics reflect p<0.05 at FDR-corrected levels (*). **D)** Bayesian model performance using different prior mean values. For each model simulation, we show the simulated vs observed RMSE for each participant (Left) and the pattern of RMSE across t_{TTC}. The model simulation with a prior mean value equal to the average across sampled durations (0.82 s) displayed a quadratic RMSE pattern across t_{TTC} that most resembled participants' observed behavior. Separate regression lines are plotted for each participant. t_{TTC} are color coded. Grey diagonal dashed line represents the identity line. Better model performance can also be observed as greater overlap between the individual regression lines and the identity line. Magenta vertical dashed line represents the scaled prior mean value used in the model simulation. **BCD)** Single-participant data plotted as dots.

pmEC hexadirectional modulation aligned to pmEC grid orientation

One-tailed one-sample Wilcoxon signed-rank tests						
Target TTC	n	V statistic	p	p_{FDR}	Effect size (r)	CI
0.55	34	286	0.580	0.908	-0.04	[-0.35, 1]
0.67	34	220	0.908	0.908	-0.26	[-0.53, 1]
0.86	34	448	0.004	0.018	0.51	[0.23, 1]
1.2	34	224	0.896	0.908	-0.25	[-0.52, 1]
Two-tailed paired Wilcoxon signed-rank tests						
Target TTC	n	V statistic	p	p_{FDR}	Effect size (r)	CI
0.86 vs. 0.55	34	425	0.029	0.023	0.43	[0.07, 0.69]
0.86 vs. 0.67	34	441	0.013	0.022	0.48	[0.14, 0.72]
0.86 vs. 1.2	34	439	0.014	0.022	0.48	[0.13, 0.72]

Table S1: Independent ROI analysis for 6-fold symmetry in pmEC

preSMA n-fold modulation aligned to pmEC grid orientation

One-tailed one-sample Wilcoxon signed-rank tests					
Target TTC	Symmetry	n	V statistic	p	Effect size (r)	CI
0.86	4	34	363	0.135	0.22	[-0.10, 1]
0.86	6	34	422	0.016	0.42	[0.12, 1]
0.86	8	34	165	0.989	-0.45	[-0.67, 1]

Table S2: Independent ROI confirmatory analyses for 6-fold symmetry in preSMA.

A) pmEC 4-fold symmetry control

One-tailed one-sample Wilcoxon signed-rank tests						
Target TTC	n	V statistic	p	p_{FDR}	Effect size (r)	CI
0.55	34	305	0.453	0.868	0.03	[-0.29, 1]
0.67	34	295	0.520	0.868	$-8.4x10^{-3}$	[-0.32, 1]
0.86	34	259	0.745	0.868	-0.13	[-0.42, 1]
1.2	34	232	0.869	0.868	-0.22	[-0.50, 1]

B) pmEC 8-fold symmetry control

One-tailed one-sample Wilcoxon signed-rank tests						
Target TTC	n	V statistic	p	p_{FDR}	Effect size (r)	CI
0.55	34	269	0.688	0.694	-0.10	[-0.40, 1]
0.67	34	312	0.407	0.694	0.05	[-0.27, 1]
0.86	34	297	0.507	0.694	$-1.7x10^{-3}$	[-0.31, 1]
1.2	34	268	0.694	0.694	-0.10	[-0.40, 1]

C) V1 6-fold symmetry control

One-tailed one-sample Wilcoxon signed-rank tests						
Target TTC	n	V statistic	p	p_{FDR}	Effect size (r)	CI
0.55	34	295	0.520	0.554	$-8.4x10^{-3}$	[-0.32, 1]
0.67	34	306	0.446	0.554	0.03	[-0.29, 1]
0.86	34	343	0.223	0.554	0.15	[-0.17, 1]
1.2	34	290	0.554	0.554	-0.03	[-0.34, 1]

Table S3: A) Independent ROI control analysis for 4-fold symmetry in pmEC. B) Independent ROI control analysis for 8-fold symmetry in pmEC. C) Independent ROI control analysis for 6-fold symmetry in V1.

A) pmEC visual grid-like modulation spatial stability

One-tailed one-sample Wilcoxon signed-rank tests						
Target TTC	n	V statistic	p	p_{FDR}	Effect size (r)	CI
0.55	34	595	$5.8x10^{-11}$	$5.8x10^{-11}$	1	[1, 1]
0.67	34	595	$5.8x10^{-11}$	$5.8x10^{-11}$	1	[1, 1]
0.86	34	595	$5.8x10^{-11}$	$5.8x10^{-11}$	1	[1, 1]
1.2	34	595	$5.8x10^{-11}$	$5.8x10^{-11}$	1	[1, 1]

B) pmEC visual grid-like modulation temporal stability

One-tailed paired Wilcoxon signed-rank tests						
Target TTC	n	V statistic	p	p_{FDR}	Effect size (r)	CI
0.86 vs. 0.55	34	429	0.004	0.012	0.53	[0.25, 1]
0.86 vs. 0.67	34	337	0.042	0.042	0.36	[0.05, 1]
0.86 vs. 1.2	34	392	0.009	0.013	0.48	[0.20, 1]

Table S4: A) Clustering of grid orientations across pmEC voxels for each TTC_i. B) Percent of pmEC temporally stable voxels for each TTC_i.

MAE for model simulations with different prior mean values

One-tailed paired Wilcoxon signed-rank tests						
Prior mean (s)	n	V statistic	p	p_{FDR}	Effect size (r)	CI
0.82 vs. 0.52	34	589	$8.1x10^{-10}$	$2.4x10^{-9}$	0.98	[0.96, 1]
0.82 vs. 0.64	34	582	$5.1x10^{-9}$	$6.4x10^{-9}$	0.96	[0.92, 1]
0.82 vs. 1.14	34	581	$6.4x10^{-9}$	$6.4x10^{-9}$	0.95	[0.91, 1]

Table S5: Comparison of group average Mean Absolute Error (MAE) across model simulations with different prior mean values

Fixation error across directions per target TTC

Mixed-Effect Model results					
Target TTC (s)	DF	F	p-value	Effect size (ϵ^2)	CI
0.55	23	0.75	0.79	$-7.5x10^{-3}$	[0.00, 0.00]
0.67	23	1.33	0.14	$9.6x10^{-3}$	[0.00, 0.00]
0.86	23	1.31	0.15	$9x10^{-3}$	[0.00, 0.00]
1.2	23	0.98	0.48	$-4.5x10^{-4}$	[0.00, 0.00]

Table S6: Fixation error across directions per target TTC.